Universidade de Aveiro
Departamento de Electrónica, Telecomunicações e Informática,
2019

Daniel Ranzal Albergaria

Free-Space Optics for Ultra-High-Speed Wireless Communications

Comunicações Óticas de Alto Débito em Espaço Livre

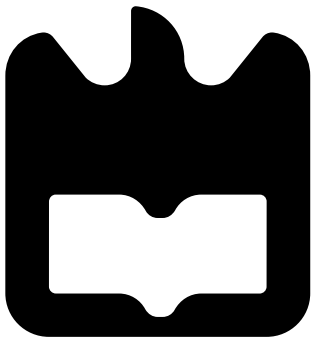

Daniel Ranzal Albergaria

Comunicações Óticas de Alto Débito em Espaço Livre

Dissertação apresentada à Universidade de Aveiro para cumprimento dos requisitos necessários à obtenção do grau de Mestre em Eletrónica e Telecomunições, realizada sob a orientação científica do Prof. Dr. Paulo Miguel Nepomuceno Pereira Monteiro, Professor do Departamento de Eletrónica Telecomunicações e Informática da Universidade de Aveiro e do Dr. Fernando Pedro Pereira Guiomar, Investigador do Instituto de Telecomunicações

o júri / the jury

Presidente / President	**Professor Doutor José Carlos Esteves Duarte Pedro** Professor Catedrático da Universidade de Aveiro
Vogais / Examiners Committee	**Professor Doutor Henrique Manuel de Castro Faria Salgado** Professor Associado da Universidade do Porto
	Professor Doutor Paulo Miguel Nepomuceno Pereira Monteiro Professor Associado da Universidade de Aveiro (orientador)

Agradecimentos / Acknowledgements

Primeiramente gostaria de agradecer todo o apoio e conhecimento fornecidos pelo meu orientador Prof. Dr. Paulo Monteiro, pelo meu co-orientador Dr. Fernando Guiomar e pelo Dr. Abel Lorences-Riesgo, a sua ajuda permitiu uma grande evolução do trabalho desenvolvido ao longo deste percurso. Gostaria de agradecer também à equipa técnica do Instituto de telecomunicações, em especial ao apoio técnico providenciado pelo João Miguel da Gama Gomes Prata.

Agradeço o apoio dos meus amigos e em especial dos meus colegas, Marco Fernandes, Miguel Carretos, Bruno Brandão e um especial agradecimento ao Fedeerico Rocco e à Beatriz Oliveira com quem pude absorver muito conhecimento.

Agradeço o apoio incondicional da minha familia e amigos, em especial dos meus pais que sempre se disponibilizaram para me auxiliar em todas as tarefas do quotidiano.

Este trabalho é financiado pelo Instituto de Telecomunicações, pelo Fundo Europeu de Desenvolvimento Regional (FEDER), através do Programa Operacional Regional do Centro (CENTRO 2020) do Portugal 2020, e Apoio Financeiro Publico Nacional (FCT) (OE; Projeto ORCIP, CENTRO-01-0145-FEDER-022141.

Palavras-chave Ótica de espaço livre, Comunicação ótica sem fio, Modelação probabilística de constelação, Modelação em tempo real de ótica de espaço livre exposta a condições atmosféricas, Direcionamento mecânico de feixes, Modulação adaptativa.

Resumo Atualmente, a distribuição de sinais por meio de canais de alta capacidade é um requisito cada vez mais crucial. Nesse sentido, a progressiva introdução de novas tecnologias de acesso móvel de quinta geração desempenha um papel fundamental, fomentando a necessidade de desenvolver novas técnicas de transmissão de alto débito para redes de fronthaul e/ou backhaul.

As distribuições de fibra estão bem disseminadas entre os países desenvolvidos, no entanto, existem algumas áreas que não sustentam esse tipo de recurso, o que é comum em regiões de baixa densidade de clientes residenciais. Para combater a ideia de que os recursos são alocados apenas nas grandes áreas, a ótica de espaço livre apresenta uma solução adequada. Alternativamente, devido à facilidade e rapidez de instalação, as comunicações óticas de espaço livre podem ser utilizadas como alternativa à fibra em casos de destruição da mesma. A comunicação ótica em espaço livre é um tipo de comunicação direcional que requer linha de vista, sendo a atmosfera o meio de propagação. Devido às variações atmosféricas, as comunicações oticas de espaço livre sofrem atenuação variável.

No decorrer deste trabalho, a interação atmosférica é objeto de estudo. Para realizar a otimização do canal de transmissão, várias alternativas são estudadas, baseando-se na previsão de canais em tempo real em conjunto com modulação probabilística da constelação. Um espelho côncavo equipado com sistema de posicionamento é também usado para superar as vibrações e outras fontes de erro posicional. No laboratório, os processos de estimativa são usados para adaptar uma conexão 64-QAM com taxas de transmissão entre 400 Gbit/s e 500 Gbit/s. O ganho do uso da modulação adaptativa é avaliado face a formatos de modulação fixos. No último estágio, o sistema de posicionadores é também testado, com o intuito de avaliar o seu impacto na estabilidade do canal.

Abstract

Signal distribution through high capacity links is nowadays a requirement that is becoming more crucial than ever. Therefore, the introduction of fifth generation mobile networks lead to the need for high capacity fronthaul and backhaul. Fiber distributions are commonly available in developed countries, however there are some areas that do not sustain this type of resource, such as in areas with low residential user density. To overcome the idea that resources are allocated only in these areas, free space optics (FSO) present a suitable and lower cost solution and can be used in temporary events (e.g. when the fiber is disrupted). Free space optics is an optical type of communication that requires line of sight, where the atmosphere is the transmission medium. Due to changes in the atmospheric conditions, free space optics systems suffer from variable attenuation.

In the scope of this work, the atmospheric interaction is the subject of study. To accomplish link optimization, several alternatives are studied, being based on channel prediction along side with probabilistic constellation shaping. A concave mirror together with a positioning system is also used to overcome structure sway and other sources of pointing error. In the lab, the estimation processes are used to produce 64-QAM connection with variable transmission rates between 400 Gbit/s and 500 Gbit/s and the gain from using adaptive modulation is evaluated. In the last stage, an automatic gimbal positioning system is also tested for several control algorithms.

Contents

Contents i

List of Figures iii

List of Tables v

Acronyms viii

1 Introduction 1
- 1.1 Communication Technology Evolution . . . 1
- 1.2 Objectives . . . 2
- 1.3 Structure . . . 3
- 1.4 Contributions . . . 3

2 Free Space Optics 5
- 2.1 Description . . . 5
- 2.2 History . . . 5
- 2.3 Modulation . . . 6
- 2.4 FSO Applications . . . 8
- 2.5 Record Performances . . . 9
- 2.6 FSO Atmospheric Interactions . . . 9
  - 2.6.1 Absorption . . . 9
  - 2.6.2 Scattering . . . 10
  - 2.6.3 Beam misalignment . . . 13
- 2.7 Wavelength Selection . . . 14

3 Characterization and Modeling of Link Loss for an Outdoor Free-Space Optics Transmission System 17
- 3.1 Introduction . . . 17
- 3.2 Experimental Setup . . . 17
- 3.3 Estimators Description . . . 18
  - 3.3.1 Moving Average with Fixed Memory Depth . . . 19
  - 3.3.2 Moving Average with Feedback and Proportional Derivative Terms . . . 20
  - 3.3.3 Moving Average with Adaptive Memory Depth, Feedback and Proportional Derivative Terms . . . 21
- 3.4 Experimental Results . . . 21
  - 3.4.1 Conclusions . . . 25

4 Adaptive Modulation **27**
4.1 Experimental Setup . . . 27
4.2 Experimental Results . . . 29
4.2.1 Adaptive Modulation Performance with Rain Conditions . . . 29
4.3 Conclusions . . . 31

5 Mechanical Beam Steering **35**
5.1 Experimental Setup . . . 35
5.2 Positioning System . . . 37
5.2.1 Mechanical Design . . . 37
5.3 Beam Characterization . . . 38
5.4 Proceeding for the Motor Alignment . . . 39
5.4.1 Blind Search . . . 41
5.4.2 Fine Tuning . . . 42
5.5 Indoor Automatic Alignment . . . 43
5.5.1 Fixed Step Correction . . . 43
5.5.2 Proportional Integral Derivative (PID) . . . 44
5.5.3 Adaptive Correction Based on Beam Characterization . . . 45
5.6 Conclusions . . . 46

6 Conclusions and Future Work **51**
6.1 Conclusions . . . 51
6.2 Future Work . . . 51
6.2.1 Free Space Optics Weather Modeling . . . 51
6.2.2 Implement an Hybrid FSO and VLC System . . . 52
6.2.3 FSO Wireless Power Transmission (WPT) . . . 52
6.2.4 Underwater Communications . . . 52

References **55**

List of Figures

1.1 USA bandwidth demand over ten years in student housing [1] 1

2.1 OOK modulated signal [15] 6
2.2 Amplitude shift keying four amplitude levels [16] 6
2.3 Quadrature Phase Shift Keying and Differential Phase Shift Keying [18] 7
2.4 Spectral efficiency for several modulation formats and number of constellation points [19] 8
2.5 Atmosphere absorption model [26] 10
2.6 Simulated scintillation impact on direct and homodyne detection effect [27] . . 10
2.7 Fog modeling accuracy for several wavelengths in four countries [30] 11
2.8 Fog attenuation for visibility until 1 km visibility [4] 12
2.9 Rain rate DSD dependency [33] 13
2.10 Rain modeling accuracy [33] 14
2.11 Auto-alignment array scheme [34] 15

3.1 Free-space optics experimental setup 18
3.2 Channel behaviour for sun and rain conditions 18
3.3 Normalized self-correlation for sun and rain 19
3.4 Received optical power (blue) and respective estimation (red) using the proposed optical power tracking algorithms. Left: data obtained during stable sunny weather conditions; Right: data obtained during unstable rainy weather conditions. 20
3.5 Memory depth during experiment 22
3.6 Estimation results with MA-adaptive-feedback algorithm sun period 23
3.7 Estimation results with MA-adaptive-feedback algorithm for rain period 24
3.8 Estimation results for sunny conditions (zoomed in) 24
3.9 Estimation results for rainy conditions (zoomed in) 25

4.1 PCS symbol probability distribution [41] 28
4.2 Adaptive Modulation Setup [42] 28
4.3 Measured SNR from the processed received signal and corresponding estimated SNR following the prediction rule. 30
4.4 NGMI for PCS-64QAM signal carries 400 Gbit/s and 500 Gbit/s 30
4.5 NGMI when adaptive PCS is applied 31
4.6 Instantaneous transmitted bit-rate with fixed and adaptive modulation 32
4.7 Accumulated capacity gain (in Terabytes) obtained by time-adaptive modulation over fixed modulation. 32

5.1 Experimental setup for indoor optimization of an automatic FSO alignment system. . . . 36
5.2 Positioning system architecture . . . 37
5.3 Trajectory definition for the two stepper motors (horizontal and vertical axes) in order to characterize the impact of pointing errors on the received optical power (see Figure 5.4). . . . 38
5.4 Power Distribution as a function of displacement . . . 39
5.5 Attenuation as a function of displacement . . . 40
5.6 Block diagram of the proposed 3-staged FSO alignment scheme. . . . 40
5.7 MATLAB-based application interface for automatic FSO alignment. . . . 41
5.8 Algorithm flow . . . 42
5.9 Induced perturbation - Fixed step correction perturbation vectors . . . 44
5.10 Received optical power over time with periodically random induction of pointing errors (red markers) and respective compensation through automatic alignment using fixed step correction (blue solid line). . . . 45
5.11 Received optical power over time with periodically random induction of pointing errors (red markers) and respective compensation through automatic alignment using the PID algorithm of expression(5.6) (blue solid line). . . . 46
5.12 Received optical power over time with periodically random induction of pointing errors (red markers) and respective compensation through automatic alignment using the LUT-aided adaptive correction algorithm (blue solid line). . . . 47
5.13 Received optical power over time with periodically random induction of pointing errors (red markers) and respective compensation through automatic alignment using a dual-state LUT-aided adaptive correction algorithm (blue solid line). . . . 48

6.1 Last mile access with FSO and VLC [47] . . . 52
6.2 Wireless power transfer technologies [48] . . . 53
6.3 Water absorption spectrum [51] . . . 54

List of Tables

3.1 2 Hour sunny day data 21
3.2 3 Hour Rainy Data 22

5.1 Positioning algorithms overview 49

Acronyms

AIR Achievable information rate.

ASK Amplitude shift keying.

ATP Acquisition tracking and pointing.

AWG Arbitrary waveform generator.

AWGN Additive white gaussian noise.

BER Bit error rate.

CCD Charge coupled device.

DD Direct detection.

DLR German aerospace center.

DPPM Differential pulse position modulation.

DPSK Differential phase shift keying.

DQPSK Differential quadrature phase shift keying.

DSD Droplet size distribution.

DSP Digital signal processing.

ECL External cavity laser.

ECOC European conference on optical communications.

EM Electromagnetic.

FEC Forward error correction.

FSO Free space optics.

HD High definition.

IEC International electrotechnical commission.

IP Internet protocol.

IR Infrared.

LDPC Low-density parity-codes.

LOS Line of sight.

LUT Look up table.

MA Moving average.

MSE Mean squared error.

NGMI Normalized generalized mutual information.

NRZ Non-return to zero.

OEO Optical electrical optical.

OOK On-off keying.

PCS Probabilistic constellation shaping.

PID Proportional integral derivative.

POE Power over ethernet.

PPM Pulse position modulation.

PSTN Public switched telephone network.

PWM Pulse width modulation.

QAM Quadrature amplitude modulation.

QPSK Quadrature phase shift keying.

RF Radio frequency.

RMSE Root mean squared error.

RoF Radio over Fiber.

SDR Software defined radio.

SNR Signal-to-noise ratio.

TCP Transmission control protocol.

TV Television.

UOWC Underwater optical wireless communications.

UUV Unmanned underwater vehicles.

VLC Visible light communication.

WDM Wavelength division multiplexing.

WOC Wireless optical communication.

WPT Wireless power transmission.

WSN Wireless sensor network.

Chapter 1

Introduction

1.1 Communication Technology Evolution

In the beginning, communication simply meant the passage of short messages or voice dialogues. However, with the passage of time the concept evolved. Nowadays, communication implies higher data streams [1], resultant from new types of services. Standard users make use of services like video call, social network access with high definition (HD) images and videos among many other features. Figure 1.1 shows that, for student housing, the required bandwidth has been increasing in the last ten years for the same number of subjects. This implies a direct increase in bandwidth per user. The study refers to a specific type of user that might be more internet dependent than the average user, however it compels the expected tendency. Combining both user and bandwidth per user increase, it is inevitable that service

YEAR	PER USER	200 USERS	500 USERS	SCALE
2011	29	116	290	Mbps
2012	43	174	435	Mbps
2013	65	261	652	Mbps
2014	98	391	978	Mbps
2015	147	587	1,468	Mbps
2016	220	880	2,202	Mbps
2017	330	1,321	3,303	Mbps
2018	495	1,981	4,954	Mbps
2019	743	2.972	7,432	Mbps
2020	1,114	4,459	11,148	Mbps

Figure 1.1: USA bandwidth demand over ten years in student housing [1]

providers experience difficulties that motivate high bandwidth technologies.

Communication industry experienced high demands in terms of throughput and suitability. Some are suited to remote areas, others are prepared for high load scenarios, such as highly populated cities with high population density and therefore there are different situations that

need personalized solutions to guarantee the best cost-performance relation.

Optical fiber is nowadays ubiquitous in nearly every sector of the global network (access, metro and long-haul), owing to its large bandwidth, low attenuation, allowing for reliable long distance communications without the need for intermediate signal regeneration.

Wireless radio frequency (RF) communications are also well spread in the market, as they can provide omnidirectional connectivity and ease of access. However, the associated cost of spectrum exploitation is immense, making it only accessible to large telecom operators. As this alternative requires high investment, its application in rural areas needs an intensive study to grant revenue [2].

Another way of reaching a high amount of users is the copper based network. Despite being well spread through the world, it is progressively becoming obsolete due to the growing needs at user level that exceeds the network available resources.

Among all the techniques mentioned before, there are some shortcomings in each technique, either the cost associated or its inefficiency. The diversity of solutions reflects the existence of different needs, however, in practice, there are some situations that could take advantage from an optimized cost-performance relation. As a suitable objector, free space optics (FSO) applied to ultra-high speed wireless communications is the subject of study in this thesis. Such technique can provide high-speed, low-cost at both implementation and maintenance, as well as ease of deployment. Owing to its inherent advantages, FSO can potentially be used in many applications, such as, last mile access, fiber backup, backhaul from antenna tower to public switched telephone network (PSTN) [3].

Atmospheric interactions play an important role as they can affect the communication link. Some studies try to model this type of interaction. However, the complexity of creating models that address all the variables that interact with the channel is an obstacle for some types of connection. There is a tendency to address system modeling under laboratory conditions, addressing controlled atmospheric interference (see e.g.[4]). The need for clear line of sight between, receiver and transmitter, the impact of scattering, scintillation, atmospheric turbulence and pointing errors are subject of study in following chapters.

1.2 Objectives

The main goals of this thesis can be summarized as follows:

- Experimentally validate an outdoor FSO communication system capable of transmitting >400 Gbit/s net bit-rate over more than 50 m and operating for long time periods.
- Implement an adaptive time-domain scheme to optimize the transmission rate accordingly to the channel conditions.
- Produce a beam characterization setup based on high resolution motors.
- Test the impact of mechanical beam steering with and without induced misalignment in long term measurements.
- Develop and experimentally validate an automatic alignment apparatus to compensate for the impact of pointing errors.

1.3 Structure

This document is organized in six chapters, with the following order:

- Introduction
- Free space optics
- Characterization and modeling of link loss for an outdoor free-space optics transmission system
- Adaptive modulation
- Mechanical beam steering
- Conclusions and future work

In the next chapter the FSO system is described, the main modulation formats are presented. Hypothetical applications are explored as well as some record performances.

The third chapter is dedicated to a thorough analysis of atmospheric impairments on FSO communications resorting to outdoor link attenuation measurements. In addition, a study of low complexity real time estimation algorithms is presented. Several sets of results are obtained for different weather conditions.

Chapter 4 addresses the use of time-adaptive modulation based on probabilistic constellation shaping as a way to improve FSO channel capacity and resilience. Real time adaptive modulation is driven by the link loss estimation methods presented in previous chapter.

The fifth chapter presents an experimental setup responsible for implementing mechanical beam characterization and steering. The main objective is to suppress misalignment in long term measurements, using two high precision motors, forming a gimbal positioning system. Several compensation techniques are implemented.

Finally, chapter six presents some conclusions and the implementation of weather modeling is proposed. Hybrid FSO and visible light communications (VLC) is also suggested. Wireless power transmission (WPT) through FSO is briefly discussed and the potential to explore underwater communications is also considered.

1.4 Contributions

The work developed in the next sections encompasses concepts in the following fields:

- Real time modulation of atmospheric conditions applied to free space optics.
- Probabilistic constellation shaping applied to free space optics.
- Mechanical beam characterization of 1550 nm free space optics.
- Mechanical beam steering applied to free space optics.

It also led to two publications:

- Paper presented in Lisbon in June, 26-28 2019 at the ConfTele conference, entitled "Characterization and Modeling of Link Loss for an Outdoor Free-Space Optics Transmission System"

- Co-author on a paper devoted to "High-Capacity and Rain-Resilient Free-Space Optics Link Enabled by Time-Adaptive Probabilistic Shaping", at ECOC, in Dublin, 24, September 2019.

Chapter 2

Free Space Optics

2.1 Description

FSO is a technology that typically requires line-of-sight (LOS) between transmitter and receiver in order to establish communication. A laser diode produces a coherent light beam whose propagation medium is the atmosphere. The atmosphere can experience variations and assume a huge diversity of states [5] directly impacting link status. However, unlike fiber, it has low deployment cost and time.

In order to facilitate LOS and thereby reduce the probability of an object intersecting communication, FSO systems are most commonly installed on top of towers or high buildings. At the transmitter, the signal generator is connected to the collimator throught an optical fiber, or it can be directly collimated if the laser is modulated. In alternative the collimator can be excluded, resulting in beam divergence. The collimator is specific to the wavelength used for the communication. At the receiver, the light wave is collected and processed with a digital signal processor (DSP) block.

As the spectrum is not licensed, the light wave can be in the visible or non-visible region. The main restrictions are standardized by International Electrotechnical Commission (IEC) [6]. The material used can be relocated allowing for setup re-utilization, thus it might require an investment inherent to collimator replacement, to suit the communication for different link distance, if an adjustable focus collimator is used for different specified ranges [7]. These properties also suggest that temporary links can be set up to evaluate if the communication in a determined region is viable or not.

2.2 History

The first notable experiment with FSO-based communications dates back to the late nineteenth century, when Alexander Graham Bell invented the photophone [8]. This invention allowed to modulate sound waves on top of an optical carrier. At the receiver many substances were tested and proved to reach to the received light beams, thereby allowing to demodulate the transmitted sound wave [9]. The experiments led to almost a quarter of mile of transmission distance [10].

During the war, the communication breakthroughs played an important role as German, British and some other forces started to use the heliograph [11]. The heliograph made use of sun light and mirrors to produce and transmit flashes carrying information. In world war two

(WWII), Carl Zeiss used the photograph principle of communication in anti-aircraft defenses [12].

Nowadays, FSO finds several commercial applications, (e.g. inter-building connectivity, for governmental institutions and internet service providing [13]), however, they still represent a small niche of the market. Some market studies predict an economical growth both in FSO and VLC [14]. The study claims such outcome based on the several new potential FSO applications that are currently emerging and also because it can be an alternative for "overburned RF technology for outdoor networking" [14].

2.3 Modulation

On-Off keying (OOK)

This type of modulation is the simplest form of amplitude shift keying (ASK). The transmitter assumes one of two states, on or off, corresponding to one and zero respectively, as depicted in Figure 2.1. OOK is also one of the simplest modulation formats to implement. OOK is widely used in FSO systems since it can be performed by directly modulating the laser current and also because it is the most simple modulation method.

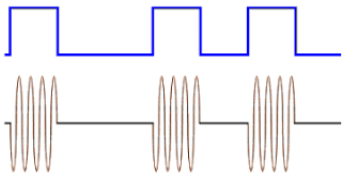

Figure 2.1: OOK modulated signal [15]

Amplitude Shift Keying (ASK)

In this modulation format, the information is carried in the amplitude levels of the carrier wave. For $M = 2^n$, there are M different symbols that can be represented by n bits. Figure 2.2 depicts an example in which four different symbols can be mapped using two bits ($M = 4, n = 2$). This alternative is slightly more complex than OOK but it is more spectrally efficient.

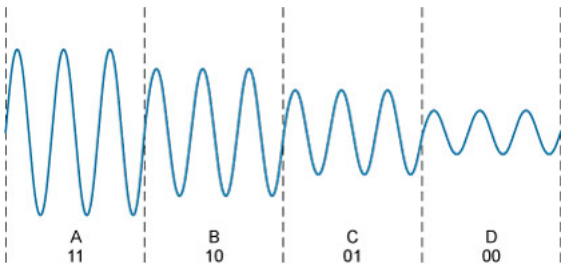

Figure 2.2: Amplitude shift keying four amplitude levels [16]

Phase-shift Keying (PSK), Differential Phase-Shift Keying (DPSK) and Quadrature Phase-Shift Keying (QPSK)

In phase-shift keying a signal is transmitted at a known frequency and information is carried in the phase. In DPSK the presence of a '1' inverts phase and in case of a '0' the phase remains.

QPSK or 4-PSK modulates the signal in phase, typically it assumes four equally spaced phases to map the symbols, composed of two bits. This methodology is highly dependent on the transceiver and the receiver synchronism as a frequency or phase mismatch might produce an error in received signal phase. By using DQPSK, a fixed phase offset between transceiver and receiver is filtered because the information is extracted not from the absolute phase, but from phase variation with respect to previous symbol. Nevertheless this strategy compares two noisy signals being that the error in one symbol can propagate to the next. An example is displayed for both QPSK and DQPSK in Figure 2.3. Typically this modulation schemes need external modulation.This modulation format is more resilient to power variations (e.g scintillation) than OOK. This is mainly due to the fact that in OOK the information is carried in a digital signal, while in PSK the information is embedded in the signal phase and therefore, irradiance variations produce less impact [17].

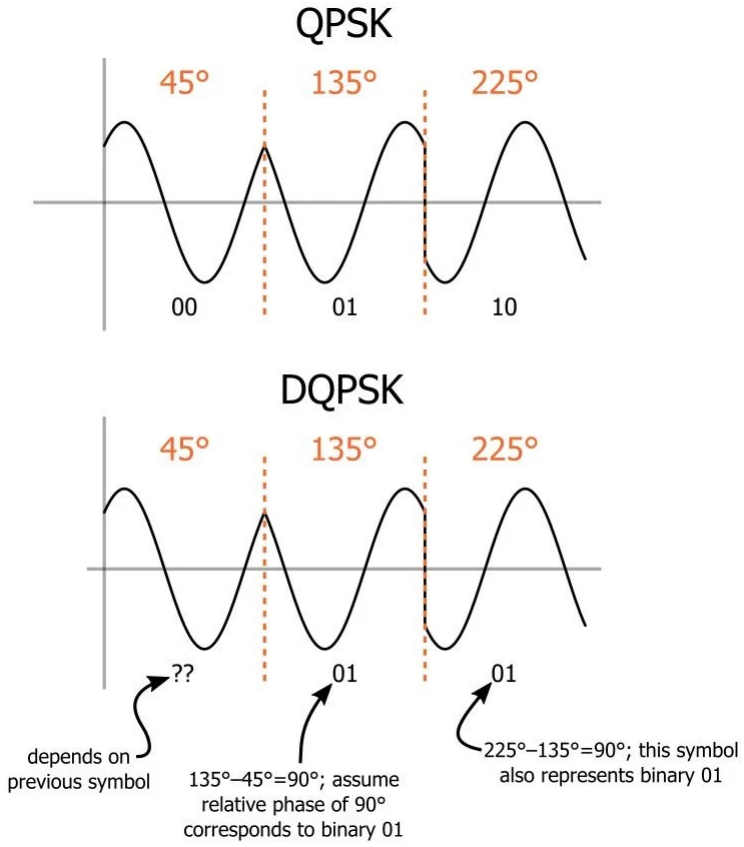

Figure 2.3: Quadrature Phase Shift Keying and Differential Phase Shift Keying [18]

Quadrature Amplitude Modulation (QAM)

QAM consists on the modulation of two orthogonal (quadrature) waves. One component is designated in-phase (I) and the other is the quadrature (Q), in-phase and in quadrature respectively, being that normally one is modulated by a sine and the other by a cosine. From the usage of this modulation, the bandwidth efficiency is increased as the information is contained both in amplitude and phase, typically this modulation scheme needs external modulation.

Some of presented modulation formats were subject of further study in [19] being proven that QAM coherent receiver performs better in terms of required SNR to achieve the same spectral efficiency, as summarized in Figure 2.4 for the modulation formats tested.

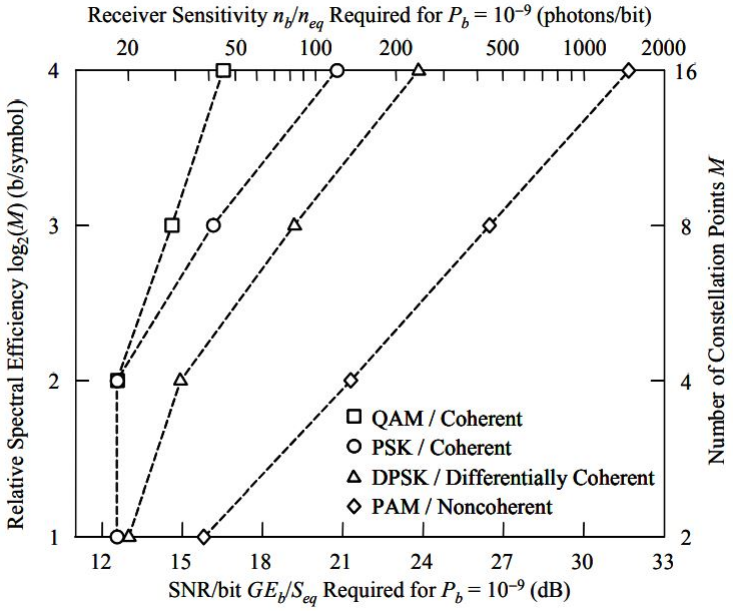

Figure 2.4: Spectral efficiency for several modulation formats and number of constellation points [19]

.

2.4 FSO Applications

Many applications are growing in diversified topics as commercial, industrial, medical and military solutions. Wireless power transmission (WPT) evolution allows for infrared (IR) power transfer to become popular [20]. The solutions are based on IR power transmission as they do not interfere with radio communication (e.g cellular and wi-fi) and the directivity promotes efficiency, even thought the alignment becomes harder.

Radio over fiber (RoF) is becoming more popular as bandwidth occupation increases. Fiber has lower attenuation, lower electromagnetic interference and reduced sensitivity to noise. However fiber does not reach certain areas. This combined with the easiness to establish a wireless optical link, allows last-mile access to be feasible with low-cost and commercially

available hardware.

2.5 Record Performances

Despite being already utilized in late 19th century, FSO technology has only made significant improvements in 21th century. Such delay in the development relates to beam steering limitations and optical-electrical-optical repeater (OEO) cost.

In 2006, a transmission record was achieved with 2×40 Gb/s system working over an aerial link [21]. At the European Conference on Optical Communications (ECOC2007), 8×40 Gbit/s transmission rate system was presented using wavelength division multiplexing (WDM). There was a report of a record transmission rate of 16×10 Gbit/s in a terrestrial link, that was presented at IEEE LEOS summer Topical Meeting, in 2008 [22]. Later in 2009 , 32×40 Gbit/s transmission record was achieved, in Italy [23].

In 2016, the German Aerospace Center (DLR) claims the world record with 1.72 Tbit/s on 3 km link, however the number of channels is not explicit [24].

2.6 FSO Atmospheric Interactions

Despite the aforementioned high data-rates, free space laser communications still suffer from many limitations. Because of reliability issues, this technology is sometimes proposed with an RF backup solution instead of a stand alone one [25]. Such proposition is made to grant link availability, even thought the RF based link grants diminished transfer rates.

The most relevant impairments come from atmospheric induced phenomena, causing attenuation that needs to be compensated in link budget. As electromagnetic waves collide with particles, two degrading interaction types are possible: absorption and scattering.

2.6.1 Absorption

Electromagnetic absorption is a process in which the molecules transform the photon energy into other types if energy (e.g heat), thus decreasing beam power. However, this produces a differentiated behaviour to different wavelengths, in Figure 2.5 the spectrum absorption to H2O, CO2, O2 and O3 is depicted for ground and 11 km level, as they constitute the majority of atmosphere. From this figure it is noticeable that some regions of spectrum present low absorption, motivating the exploitation of the 1550 nm wavelength region.

Scintillation

Scintillation is caused by temperature variations, associated to ionizing radiation absorption. It produces intensity fluctuations in the beam because of heterogeneous characteristics of atmosphere constituents. It is hard to model, typically it is studied considering statistical models that are dependent on temperature and humidity. The effect can be reduced if homodyne detection is used instead of direct detection. This results from accounting the ability of mixing the reference field introduced by the oscillator and the signal field with a square law detector [27]. Figure 2.6 depicts bit error rate (BER) as function of scintillation strength for both direct and homodyne detection. To access induced attenuation by scintillation, further analysis can be made through modified Rytov theory, for a Gaussian beam [28].

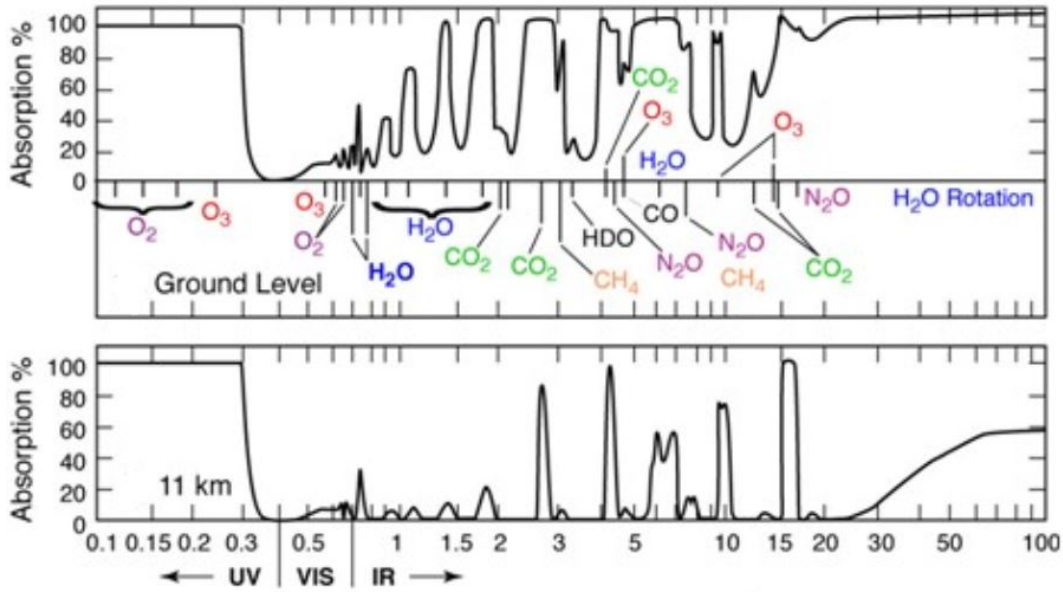

Figure 2.5: Atmosphere absorption model [26]

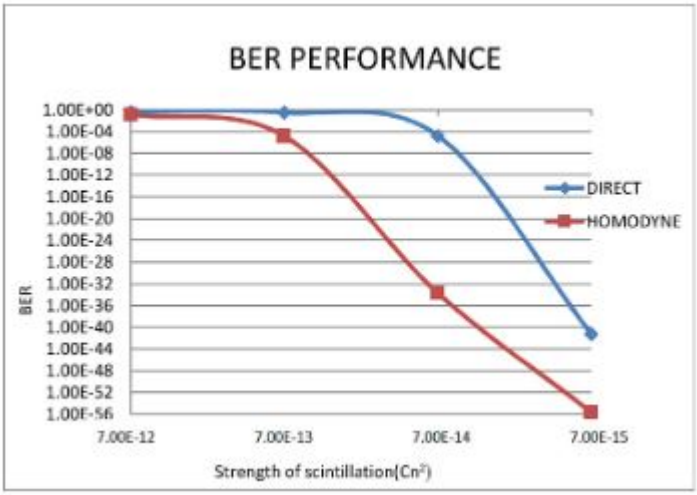

Figure 2.6: Simulated scintillation impact on direct and homodyne detection effect [27]

2.6.2 Scattering

Typically, reflection is caused by the existence of different particles, or by particles at different temperatures. As light travels, it collides with some particles and is redirected into another direction. When that occurs, it creates multiple paths, causing beam energy dispersion. Such type of phenomena is often associated to fog and rain.

Fog and Smoke

Fog is one of the most limiting phenomena for FSO communications. It is composed of water steam that can absorb light, attenuating the signal or even obstructing it. Figure 2.8 exploits wavelength dependency, attenuation results extracted with fog and smoke, as a function of visibility in kilometers. The image also shows that 1.55μm performs better when compared with 0.67 μm and 0.830 μm with fog and smoke respectively. Fog attenuation B_λ (db/km) is typically described as function of visibility (2.1),

$$B_\lambda = \frac{13}{V}\left(\frac{\lambda}{550}\right)^{-q} \tag{2.1}$$

where V is the distance (in km) for which the image distinction drops to 5% of the corresponding image if the object is nearby and q is a parameter that models the wavelength dependency according to the visibility function [29]. There are two popular models that define attenuation similarly, which differ in the way q is defined, as written in expressions (2.2) and (2.3), for Kruse and Kim estimators respectively. The Kim model is an improvement to produce better results on fog attenuation estimation.

$$q = 0.585V^{1/3}, \qquad V < 6\ km \tag{2.2}$$

$$\begin{aligned} q &= 0.16 + 0.34V \qquad 1 < V < 6\ km \\ q &= V - 0.5 \qquad\quad 0.5 < V < 1\ km \\ q &= 0 \qquad\qquad\quad V < 0.5\ km \end{aligned} \tag{2.3}$$

There are some other approaches to quantify fog that produce improved results (see Figure 2.7), however their effectiveness varies with location for the same wavelength and visibility [30], suggesting that some effects might not be accounted or that the experience might not be repeatable with the intended precision. The root mean squared error (RMSE) between the model prediction and actual measurements is still within or above the 20dB region, a strong indicator that there is still much work to be done.

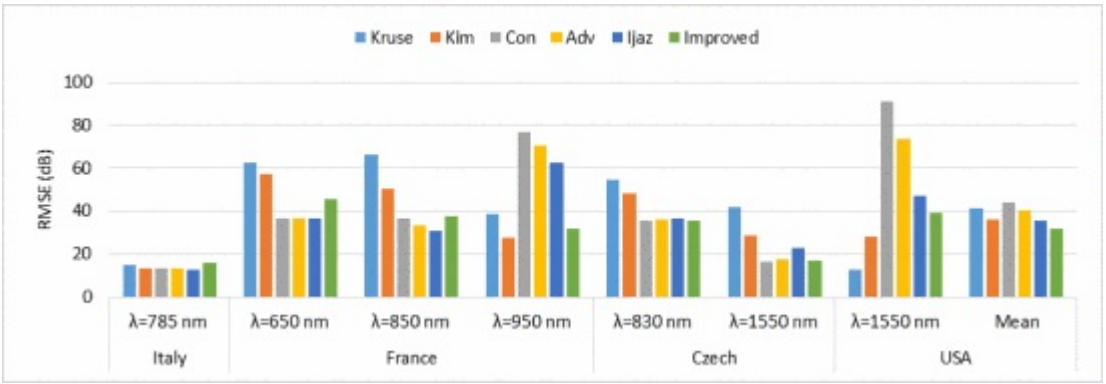

Figure 2.7: Fog modeling accuracy for several wavelengths in four countries [30]

Figure 2.8 represents attenuation as a function of visibility, demonstrating that 1550 μm tends to outperform other presented wavelengths [4].

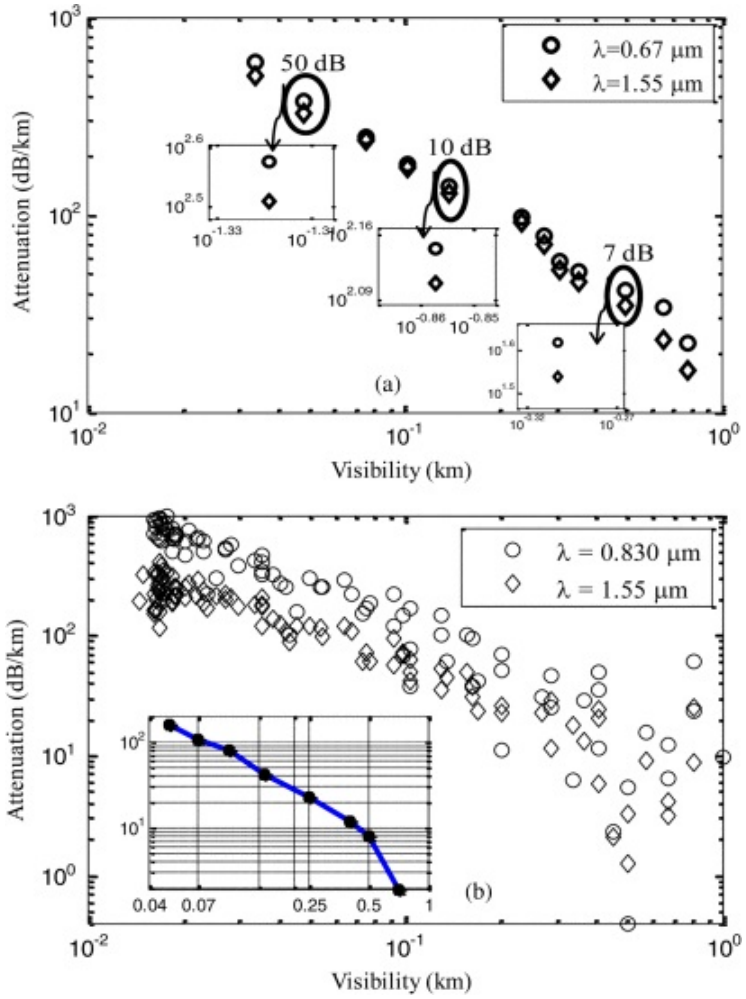

Figure 2.8: Fog attenuation for visibility until 1 km visibility [4]

Rain

Rain is a factor that is considerably present in almost every location in Europe [31]. In radio communications, it is one of the main impairments for frequencies above 10 GHz [32]. As free space optics can be used in an hybrid RF-FSO link, it is important to understand if link availability can be granted with optical communication.

Associated attenuation mainly varies due to rain rate and droplet size distribution (DSD). To exhibit that the rain induced attenuation depends also of droplet shape (μ), several droplet shape parameters are analysed, the highest (μ) values depicted in Figure2.9, correspond to increased droplet size. In Figure 2.9. For low rain rates, the attenuation is not highly dependant on the droplet properties. However for higher rain rates there is a clear dependency on the shape parameter, potentiating attenuation from 10 dB/km to 65 dB/km for a rain rate of 150 mm/h. There are some models to predict rain attenuation effect [33], such as the Lin

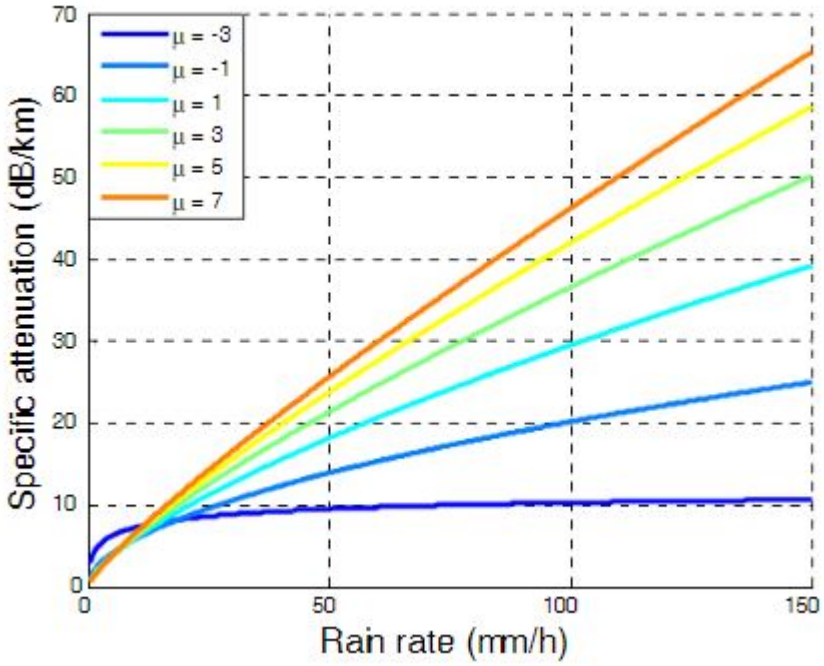

Figure 2.9: Rain rate DSD dependency [33]

model, which can be written as (2.4),

$$\begin{aligned} A(P) &= kR(P)^{\alpha}Lr \\ r &= \frac{1}{1+\frac{L}{L(R)}} \\ L(R) &= \frac{2623}{R(P)-6.2}, \end{aligned} \tag{2.4}$$

where A(P) is the attenuation as function of percentage of the yearly time, P, k and α are coefficients related to the DSD shape parameter, L is path length and r the path reduction factor. Figure 2.10 displays the RMSE associated to different models presented in [33]. From Figure 2.10 it is noticeable that Lin and Moupfouma models present better estimation for distances up to 5 km. Rain models can provide RMSE around 2%.

2.6.3 Beam misalignment

The amplitude of misalignment varies with the type of application. If a link is to be established between one or two moving objects it requires fast and high precision beam steering. In case of two fixed points, there can be relative movement due to small vibrations like building sway. If the link distance is increased, the same vibration corresponds to higher mismatch; This means that, the positioning system precision needs to be higher for higher link distances. Alignment correction experiments prove that link stability can be improved with correction algorithms such as those presented in [34]. Figure 2.11 exhibits an alignment scheme, based on detection arrays, that are used to track beam misalignment and allow to discover the positional

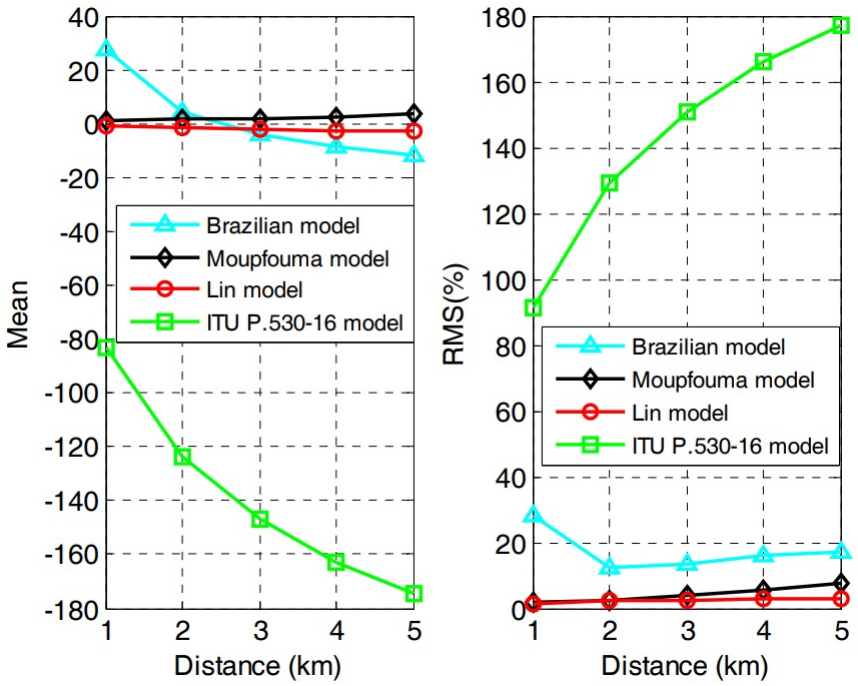

Figure 2.10: Rain modeling accuracy [33]

error associated. The effectiveness of auto-alignment algorithms is however, dependable on beam distribution. This characteristic can change with the type of dispersion of the medium, divergence angle associated to collimator lenses, the existence of beam redirectioning mirrors, among others.

2.7 Wavelength Selection

The wavelength selection, is a priority topic as it is a trade-off between transmission rate in the presence of atmospheric elements, material cost and eye safety.

As previously highlighted in Figure 2.6 there is in overall good performance at 1550 nm wavelength region, considering atmospheric interactions such as absorption and scattering.

With respect to eye safety concerns, wavelengths between 400 and 1400 nm can be harmful as the retina does not produce a blink effect, leaving the eye unprotected. However, the results produced at 1550 nm show that the cornea is able to absorb the radiation more efficiently, protecting the retina. Consequently, the maximum eye safe power can be fifty times higher [35].

In addition, the usage of the 1550 nm region for FSO communications also benefits from full compatibility with modern fiber optic communications, which typically operate within the same wavelengths. This makes it much simpler to integrate FSO with currently deployed fiber systems, enabling seamless last mile connectivity, fronthauling and backhauling without the need for complex wavelength conversion modules.

Motivated by the list of aforementioned reasons, for the remaining of this thesis we will consider FSO communications within the 1550 nm wavelength region.

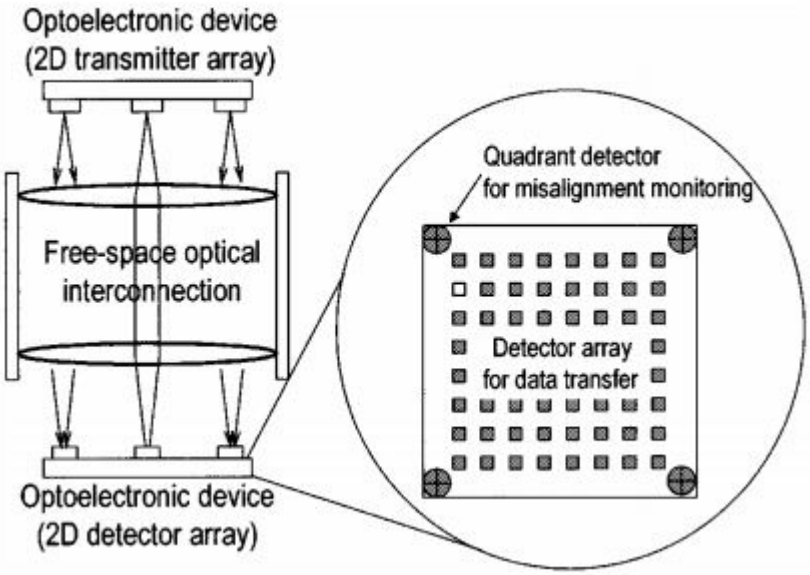

Figure 2.11: Auto-alignment array scheme [34]

Chapter 3

Characterization and Modeling of Link Loss for an Outdoor Free-Space Optics Transmission System

3.1 Introduction

Free-space optics are a suitable solution and proved to have good performance for high capacity applications, being proposed as an access network [36]. However, there is still some skepticism on using this technology due to the lack of further practical validation against the impact of inherent atmospheric phenomena in outdoor deployments. As described in the previous chapter, there are some models that try to quantify attenuation with respect to channel conditions. However, they rely on parameters that are hard to quantify, difficult to extract systematically and do not take in account all the variables. Contrary to fiber links, FSO presents a dynamic behaviour, creating time-varying link loss. This affects the power budget, impacting the ability to transmit at certain transmission rates. Despite the existence of models to quantify channel conditions, they do not sustain the idea that the channel can experience fast variations and it is hard to quantify all types of perturbations.

3.2 Experimental Setup

To validate the stability of wireless optical communication (WOC), a simple system is designed and deployed in an outdoor scenario to perform signal transmission. In this case, continuous wave is transmitted to evaluate the medium-induced attenuation.

Figure 3.1 shows the setup used for the experiment. An emitting laser at 1550 nm with +11 dBm output power is used as transmitter; the signal then propagates through fiber to a colimator with 24 mm diameter, a divergence angle of 0.0017^{o}, numerical aperture of 0.24 and focal length of 37.13 mm. At 27.5 m from the transmitter there is a concave mirror whose function is to reflect the wave into the receiver, resulting in a total link length of 55 m. The receiver is also composed of a colimator with the same specifications as the transmitter one, collecting the power received with an optical power meter with 0.25 Hz sampling rate. The power measurements are processed using MATLAB. The positioning system is manual and exposed to weather conditions; it is also worth pointing out that the lenses have no protection from the rain droplets or sun radiation.

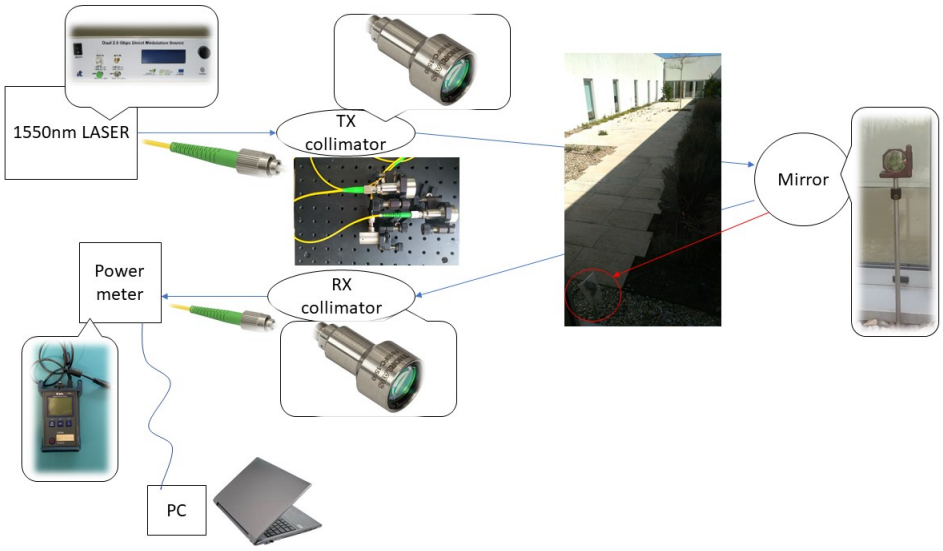

Figure 3.1: Free-space optics experimental setup

3.3 Estimators Description

FSO loss fluctuations are much higher and faster than those typically experienced in an optical fiber. To see that there is weather dependency from sun and rain, two measurements are taken, as shown in Figure 3.2 exhibits. These measurements correspond to a 2 hour sunny day period and 3 hour rainy period, with 0.25 Hz of sampling frequency. It is noticeable that channel variations occur with considerable amplitude and frequently for both cases.

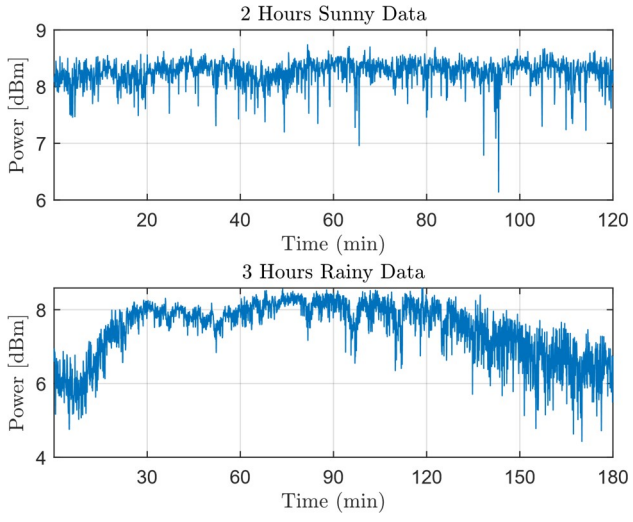

Figure 3.2: Channel behaviour for sun and rain conditions

The data set obtained under sunny weather exhibits fast variations that appear to be dominated by a random component. The received power measurements are mostly within 1 dB oscillations, with some sporadic fast fading evens reaching up to 2 dB attenuation.

Variance among samples might be the indicator of scintillation and pointing error effects, as measurements were taken in summer under high temperatures.

Unlike the sunny weather measurements, the received power collected under rainy conditions shows some clear non-random trends, which seem to be correlated with the precipitation rate. There are also two distinct power levels, one in the region of 6 dBm and another in 8 dBm region, we conjecture that it is possible that water droplets that slide through lenses might change the reflection properties of the receiver.

Figure 3.3 displays the normalized auto-correlation associated with the power measurements. The curves indicate that there is memory in the channel. The rain data set expresses larger coherence between samples, on the other end, sun has low memory depth, a clear indication of the dominance of random variations.

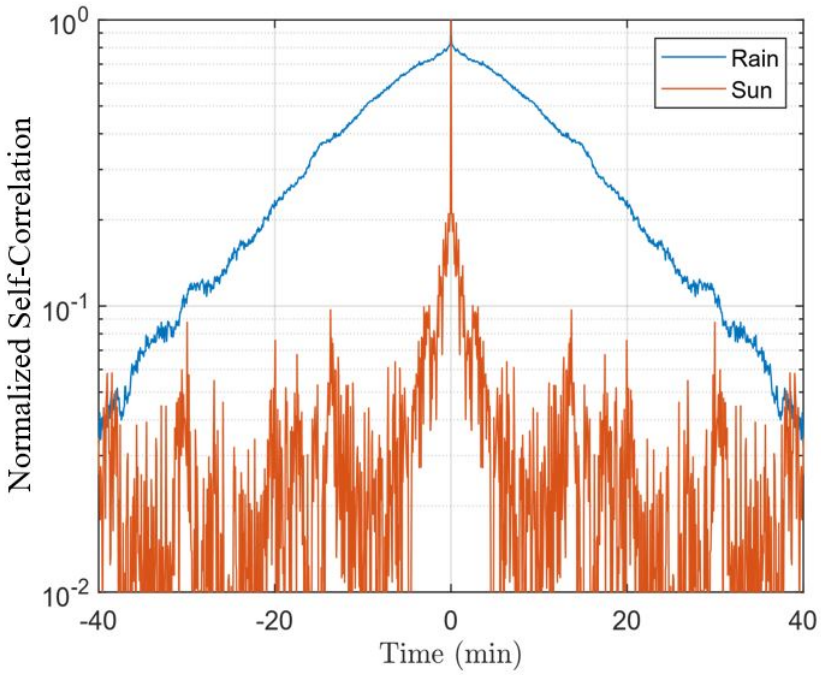

Figure 3.3: Normalized self-correlation for sun and rain

From the analysis of link behaviour, the idea that the channel has memory leads to the creation of real time prediction models, which can be based on moving average approaches. Such methodology results in low complexity operations, becoming highly attractive in the sense that computation does not take significant time, therefore not inducing sampling limitations.

3.3.1 Moving Average with Fixed Memory Depth

The baseline approach is to perform a moving average estimation (MA-fixed), as given by,

$$y(n) = \frac{1}{N_{\text{taps}}} \sum_{k=0}^{N_{\text{taps}}-1} x(n-k), \tag{3.1}$$

where N_{taps} is the number of memory taps to be included in the moving average. Based on mean squared error (MSE), estimation quality is assessed,

$$\text{MSE} = \frac{1}{N_{\text{taps}}} \sum_{n=0}^{N_{\text{taps}}} [y(n) - x(n)]^2 \,, \tag{3.2}$$

where $y(n)$ refers to the estimation and $x(n)$ is the actual measured channel condition. Figure 3.4 depicts both the signal and the estimation for the data presented earlier. The memory depth is fixed over the experiment and assumes optimized value prior to estimation process. MA-adaptive represents the estimation process with real time memory depth optimization.

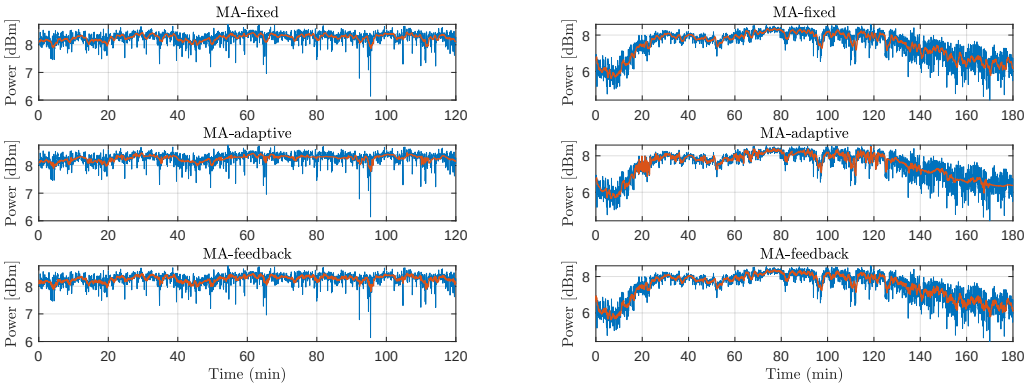

Figure 3.4: Received optical power (blue) and respective estimation (red) using the proposed optical power tracking algorithms. Left: data obtained during stable sunny weather conditions; Right: data obtained during unstable rainy weather conditions.

MA-fixed presents some limitations, the optimum memory, might not suit the channel behaviour during all experiment resulting in poor estimation as the algorithm does not track the channel conditions. If the memory depth is too high, the channel tracking becomes quasi-static, filtering high frequency variations. However, this method is of low complexity.

3.3.2 Moving Average with Feedback and Proportional Derivative Terms

Moving average with feedback and proportional derivative terms (MA-feedback) is akin to MA-fixed, with two additional terms, the increment between the past two samples and the previous estimation error. This approach presents an intent to detect the spikes and neglect them partially, resulting from the observation that there are numerous spikes that appear randomly, having mainly short-time persistence. Both the estimation error and its time derivative tend to vanish when the power is stable, assuring that there is no noise being inserted at that condition. The corresponding estimator can be written as,

$$y(n) = \frac{1}{N_{\text{taps}}} \sum_{k=0}^{N_{\text{taps}}-1} x(n-k) \frac{1}{1 + \delta(n) + \epsilon(n)}, \tag{3.3}$$

where e(n) is a feedback error component given by,

$$\epsilon(n) = (y(n-1) - x(n)) \cdot C_1, \tag{3.4}$$

and δ is the proportional derivative term,

$$\delta(n) = (x(n) - x(n-1)) \cdot C_2, \tag{3.5}$$

in which C_1 and C_2 are weighting constants. Under sunny conditions they are imposed as 0.001 and 0.0077 respectively. For rain conditions weighting constants are recalculated to $C_1 = 0.0001$ and $C_2 = 0.0260$. Constants were obtained also by performing an optimization based on prior tests.

From the derivative component and feedback there is the ability for the algorithm to change faster the prediction for the next moment, specially when a disruption or a power increase occurs. It is clear that the compensation of the error is made faster if proper weight constants are used.

3.3.3 Moving Average with Adaptive Memory Depth, Feedback and Proportional Derivative Terms

The two previous algorithms presented memory depth, which is useful to produce a response that filters high frequency components. In this algorithm (MA-adaptive-feedback) not only the feedback loop and a derivative term are imposed, but the effect of using adaptive memory depth is also included,

$$y(n+1) = \frac{1}{N_{\text{taps}}(n)} \sum_{k=0}^{N_{\text{taps}}(n)-1} x(n-k) \frac{1}{1 + \delta(n) + \epsilon(n)}. \tag{3.6}$$

3.4 Experimental Results

The results were extracted in two different conditions: sunny and rainy day. Tables 3.1 and 3.2 depict the obtained MSE, the optimized number of taps and the maximum instantaneous squared error obtained for MA-fixed and MA-feedback algorithms. The maximum instantaneous squared error is accounted for, since error spikes can endanger hypothetical communications like 5G, which have stringent requirements in terms of ultra-high reliability.

Table 3.1: 2 Hour sunny day data

Estimator	MA-fixed	MA-feedback	MA-adaptive-feedback
MSE	0.04274	0.0425	0.0315
Taps	13	13	27 avg.
Max Squared Error	3.36	3.554	2.6330

For sunny day performance, two algorithms present similar results. The number of taps is fixed to a value of 13 which resulted from prior test optimization. Even though the estimation for rainy weather shows approximately 4 times higher MSE, the corresponding maximum squared error is similar. After obtaining these results, the dependency from memory depth was evaluated in Figure 3.5.

Results show that the memory depth that provides the best performance can change drastically over time. This behaviour conveys the need to filter fast variations.

Table 3.2: 3 Hour Rainy Data

Estimator	MA-fixed	MA-feedback	MA-adaptive-feedback
MSE	0.1321	0.1297	0.0911
Taps	13	13	18 avg.
Max Squared Error	3.273	3.508	2.8879

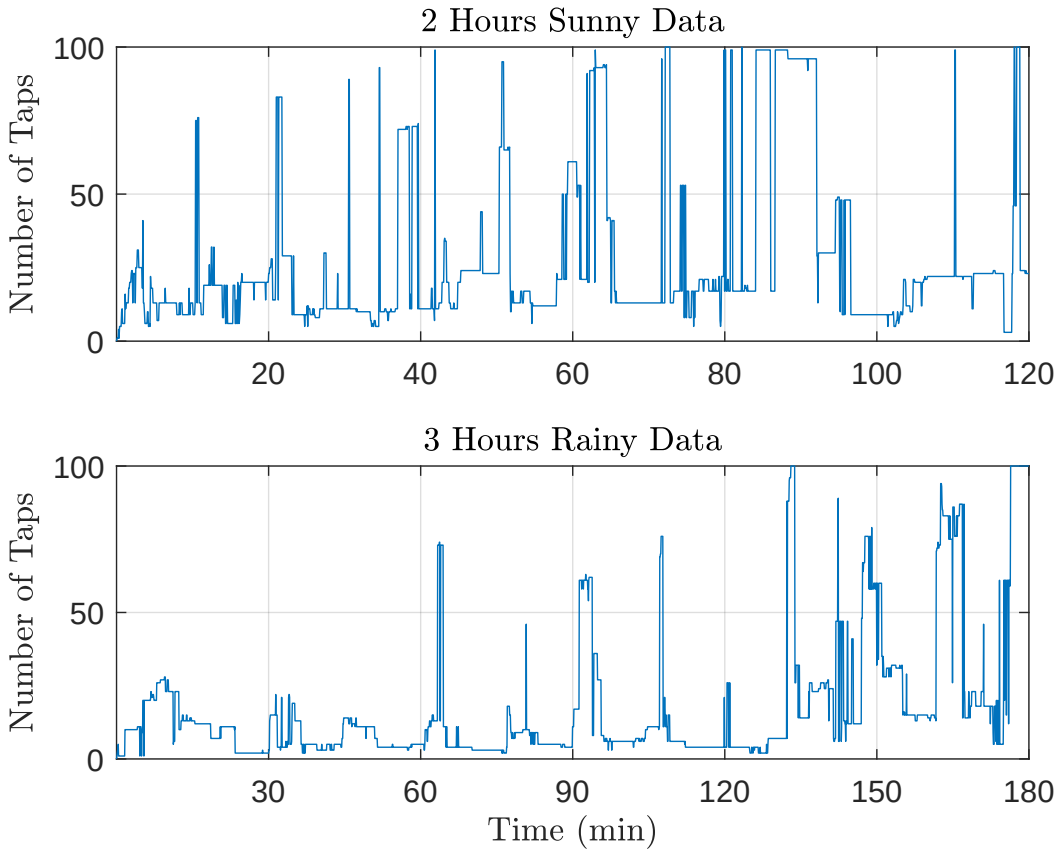

Figure 3.5: Memory depth during experiment

It is clear that sunny weather produces higher random component behaviour. By increasing the number of taps dramatically the estimation system, neglects the spikes, reproducing a low pass filter behaviour. Rainy weather presents different needs in terms of filtering, as the data contains similar behaviour among samples, the algorithm does not need to force low pass filtering. Rain data displays high number of taps in the final stage as it tries to gather samples to reduce the estimated power.

Previous results support the idea that MA-feedback can be useful in the sense that the derivative term might help neglecting the spikes that need to be compensated in sunny data and also reduce the estimation in case of disruption or high attenuation. As shown in Section 3.3.3, the idea of using adaptive memory depth was also explored. This method leads to higher complexity and processing time; however, it also increases the performance, as shown in Figure 3.6 and 3.7 and Tables 3.1 and 3.2.

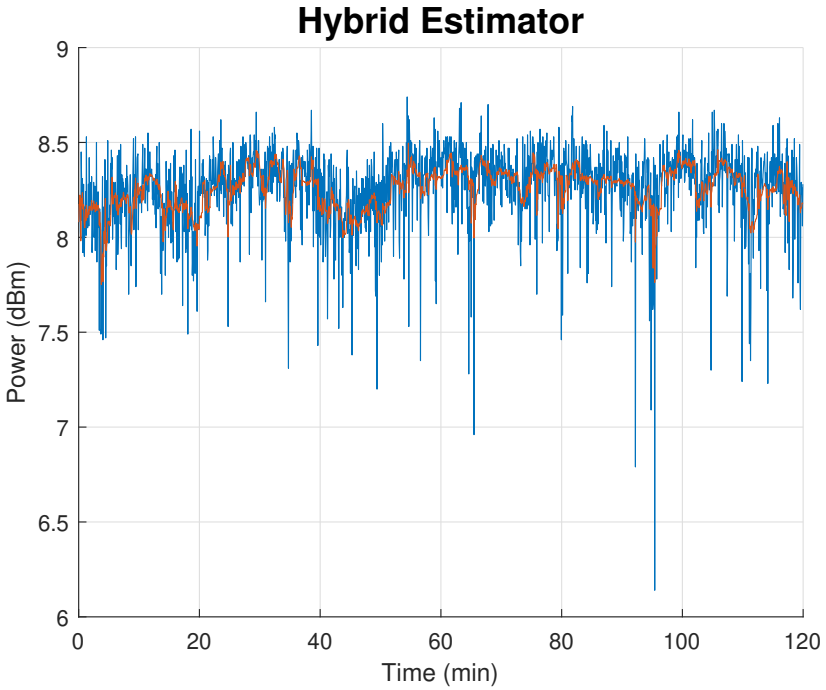

Figure 3.6: Estimation results with MA-adaptive-feedback algorithm sun period

In the presence of sunny conditions, the mean memory depth reaches 27 samples, meaning that the system filters high frequency components better, and as a result the mean squared error decreases significantly. The maximum error is also reduced, indicating that this type of prediction may lead to a higher reliability. Figure 3.8 highlights the region in which there is high variance. The algorithm shows low sensitivity to new samples, which allows the system to predict a more stable behaviour. It is also worth mentioning that attenuation bursts do not last long and therefore its neglecting was successful. The regions with low variation present more sensibility to new samples. Link improvement is also seen as an isolated behaviour and therefore it is also partially neglected.

In the presence of rain, the performance of hybrid estimation technique is improved with respect to other estimation techniques. The mean squared error is reduced by approximately

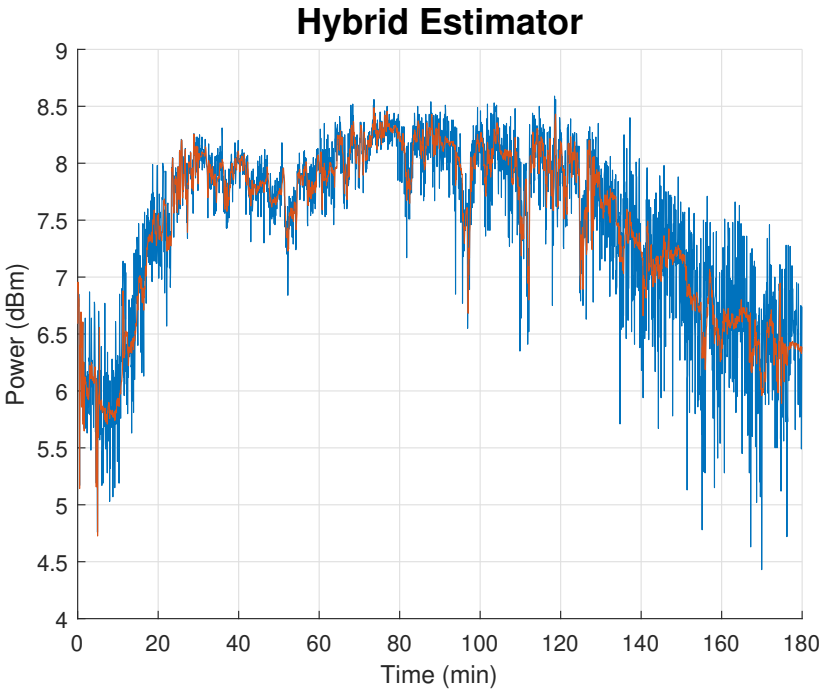

Figure 3.7: Estimation results with MA-adaptive-feedback algorithm for rain period

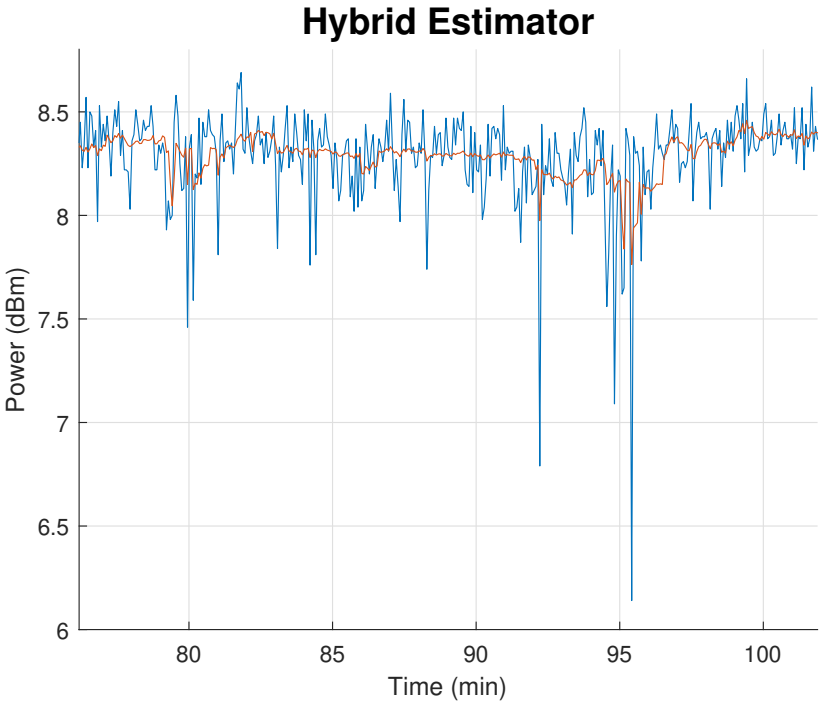

Figure 3.8: Estimation results for sunny conditions (zoomed in)

30% and the optimum average memory depth is 18 samples. The maximum squared error is also improved. During high attenuation with persistent effect Figure 3.9 shows that the estimation is able to track the trend change; this means that this can be used in diversified weather conditions without performing modifications in the algorithm coefficients.

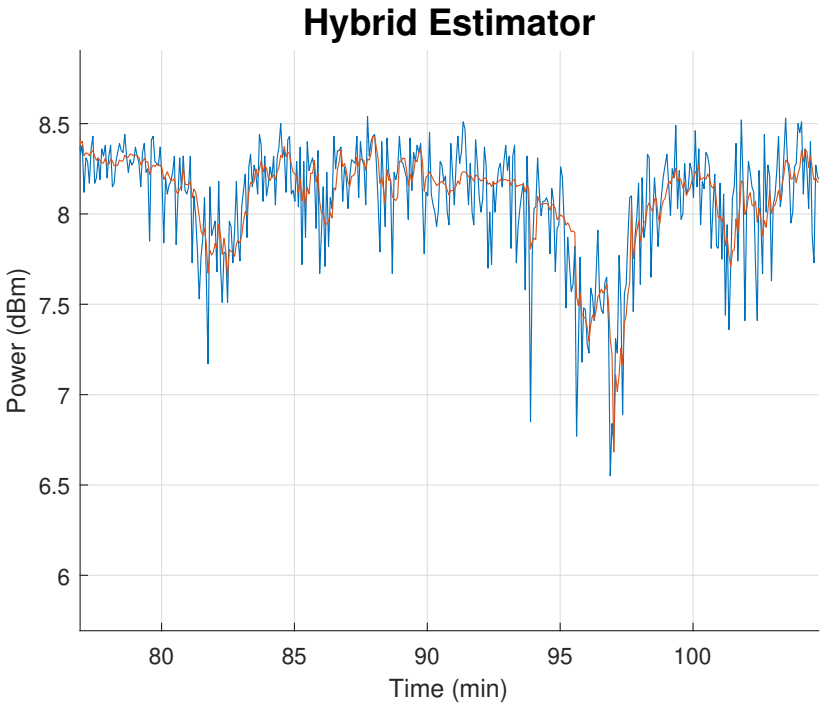

Figure 3.9: Estimation results for rainy conditions (zoomed in)

3.4.1 Conclusions

It is worth noting that even the simplest proposed estimator is able to track the FSO channel condition with high accuracy. Higher performance is achievable by increasing the computational complexity of the estimation algorithm, namely by integrating an adaptive estimation of the optimum number of taps together with proportional and derivative feedback errors. The maximum squared error can be an adequate indicator, to quantify critical estimation errors. In an hypothetical application, in which one can adapt the transmission rate according to the estimated link conditions, such critical errors can translate into communication errors. On the other hand, if the communication is more robust and independent of connection loss, an MSE minimization can provide better performance metric.

Chapter 4

Adaptive Modulation

As exposed in the previous chapters, the FSO channel on an outdoor environment can be unstable. Nevertheless, it can represent a wireless alternative to fiber in earth-to-earth applications with the ability to provide ultra-high capacity fronthauling in beyond 5G access networks. The number of effects that can produce link variations suggest that the power on the channel can vary over time. The continuous increase in number of users and volume of packages shared through the network calls for an urgent optimization of current communication systems. In the last decades, many studies were directed towards high capacity links. In this chapter, an adaptive scheme is tested to respond to FSO link variations and also to optimize throughput.

To increase transmission rates by approaching the Shannon limit, advanced forward error correction (FEC) [37] plays an important role in modern communications systems. Low-density parity-check (LDPC) and turbo-codes became popular and increased capacity usage. Such tendency also led to research in constellation shaping [38].

Probabilistic constellation shaping (PCS) uses the fact that with Gaussian distribution, the Shannon limit is approached, as it mimics additive white Gaussian noise (AWGN) capacity [39]. From such property, the channel capacity can be increased to get a gain when PCS is used instead of an uniform QAM, while allowing bit-rate adaptation with arbitrary granularity. From the ability to adjust transmitted signals by adjusting symbol probability as expressed in Figure 4.1, the signal quality can be improved and consequently produce bit-rate gain [40]. In order to optimize this modulation, it is necessary to evaluate the current link conditions: if the available signal-to-noise ratio (SNR) is high, then more information entropy (an thus higher bit-rate) can be loaded at the transmitter; otherwise, the entropy must be reduced to guarantee error free communication.

4.1 Experimental Setup

Figure 4.2 displays the set of materials used during the experiment. The baseband digital modulation at a 64 Gbaud is performed by an arbitrary waveform generator (AWG) operating at 120 Gsa/s, with 45 GHz of analog bandwidth. The adaptive bit-rate is achieved based on PCS-64QAM. The transmitted signal is composed of 20% of overhead to allow forward error correction (FEC) and 6.25 % overhead for DSP pilots. This allows a maximum entropy of 6 bit/symbol, corresponding to a maximum net bit-rate of 300 Gbit/s; because we are using dual-polarization we can achieve 600 Gbit/s.

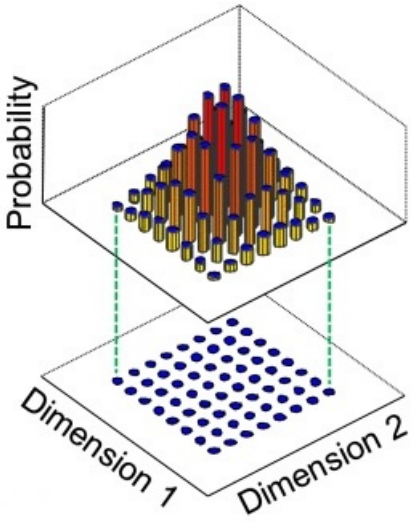

Figure 4.1: PCS symbol probability distribution [41]

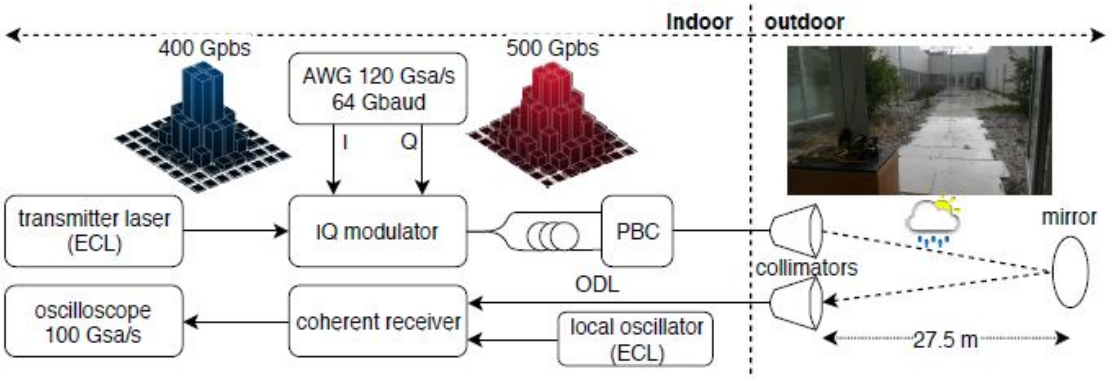

Figure 4.2: Adaptive Modulation Setup [42]

In order to maintain the transmitted power, the DSP pilots are QPSK-like symbols inserted with the average signal power. The signal is optically modulated in a single-polarization IQ modulator with 22 GHz bandwidth. An external cavity laser (ECL) emitting at 1550 nm with 100 kHz linewidth is responsible for sourcing the optical power (15 dBm). Dual polarization is achieved by using a 1 m line to introduce an optical delay leading to time decorrelate the two polarization tributaries.

In the free-space interface, the wave is expelled through one collimator with 24 mm diameter and 0.017 full-angle divergence. After 27.5 m, the beam is collected at a concave mirror with 30 m focal length and reflected for another 27.5 m resulting in a 55 m link. In the receiver, the beam is collected through a collimator of the same model as the described previously. The system is located outdoor, being completely exposed to atmospheric conditions and without any special protection. In the receiving end, a dual-polarization coherent receiver with 40 GHz bandwidth converts the optical signal into electrical domain and mixes it with a local

oscillator with 100 kHz linewidth and 13 dBm optical power.

The optical transmission is highly dependent on the power variations in FSO link as there is no amplification. To sample the I and Q components, a 4 port real-time oscilloscope is used with 100Gsa/s and 33 GHz analog bandwidth. Finaly a MATLAB script is responsible for offline DSP that compensates for channel perturbations and allows signal decoding.

4.2 Experimental Results

4.2.1 Adaptive Modulation Performance with Rain Conditions

With the estimation algorithms dissected on Chapter 3, the optimized memory depth is obtained for a small set of data corresponding to 10 minute acquisition. In order to accommodate fast variations of the FSO channel, an $\mathrm{SNR}_{\mathrm{margin}}$ of 2 dB is established and a fixed memory depth is used as predictor. The adaptive modulation scheme is updated in real time, being the main limitation the sampling period. After evaluating the optimum number of taps, a continuous measurement is taken for a 3 hour period. During each iteration, a batch of 2×10^5 samples is retrieved through the oscilloscope with 2 fixed bit rates and an adaptive bit-rate signal based on a controlled entropy loading of a PCS-64QAM constellation::

- 400 Gbit/s fixed bit rate.
- 500 Gbit/s fixed bit rate.
- Adaptive modulation with bit-rate adapted to estimated SNR.

Bit-rate adaptation is conducted by monitoring the achievable information rate (AIR), with respect to the estimated SNR and a normalized generalized mutual information (NGMI), above the pre-defined threshold ($\mathrm{NGMI}_{\mathrm{th}}$) of 0.9 [43], in order to guarantee error-free transmission with an FEC overhead of 20%. The PCS constellation size has been fixed to $M_{\mathrm{PCS}} = 64$.

As the fixed modulation formats do not require real time processing, for re-adapting the transmitted bit-rate, their waveforms are only recorded during measurement and processed afterwards. By estimating SNR and giving a 2 dB margin, the SNR curve is extracted and correlated with rain periods , as shown in Figure 4.3. It is noticeable that link suffers some major periods of instability, such was already predicted in previous chapter. To evaluate if those periods affect connection with disruptions, NGMI is also evaluated to both modulation formats 4.4.

For lower transmission rate disruption does not occur, since the required SNR to maintain the NGMI above the FEC threshold is much lower than the average link SNR. However, for 500 Gbps the number of disruptions is high, and sustains over nearly 30 min period, such is not acceptable in most forms of communication. With adaptive PCS the number of disconnections is reduced and they do not occur continuously (see Figure 4.5), being more reliable than 500 Gbit/s fixed rate. This seems to be a solution that presents a good compromise in terms of throughput. However, it still lacks reliability which can be a problem, especially for real time applications. For all considered format (fixed and adaptive), instantaneous bit-rate has been registered and is shown in Figure 4.6, evidencing that 500 Gbps can not always be accomplished and that adaptive modulation in average performs around 470 Gbps, providing a significant gain over the 400 Gbps fixed modulation rate.

Figure 4.7 displays the gain over time from using adaptive PCS when compared with the two fixed modulation formats. Most of the gain comes naturally from the when connection

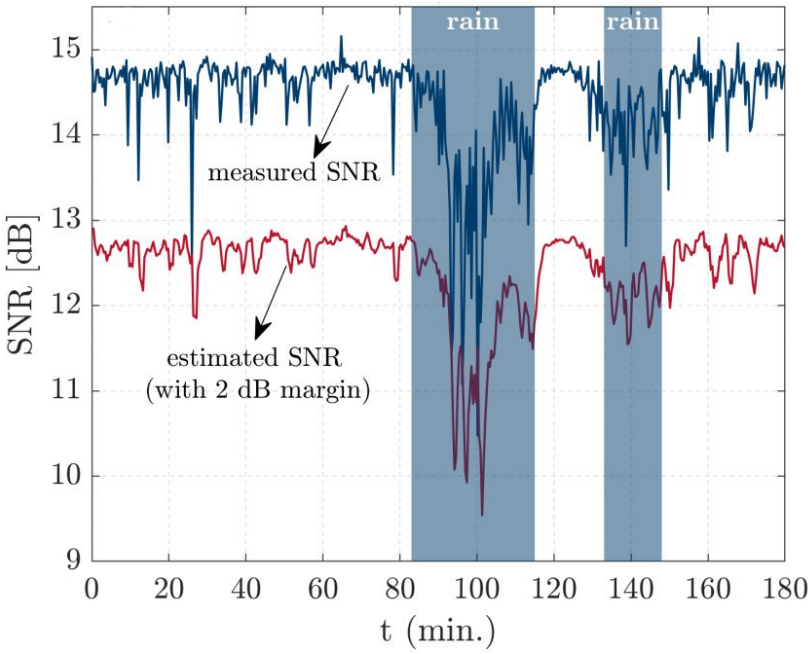

Figure 4.3: Measured SNR from the processed received signal and corresponding estimated SNR following the prediction rule.

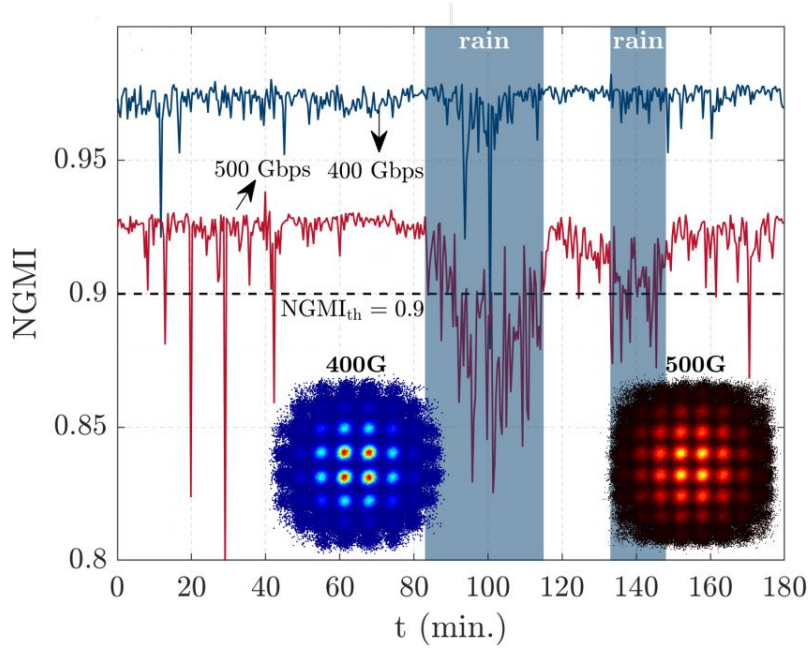

Figure 4.4: NGMI for PCS-64QAM signal carries 400 Gbit/s and 500 Gbit/s

is disrupted and the adaptive PCS scheme reacts and compensates. When the connection is stable, 500 Gbps outperforms PCS, because of the 2 dB margin that underestimates connection conditions. Even though the margin lacks optimization, there is a clear capacity gain from

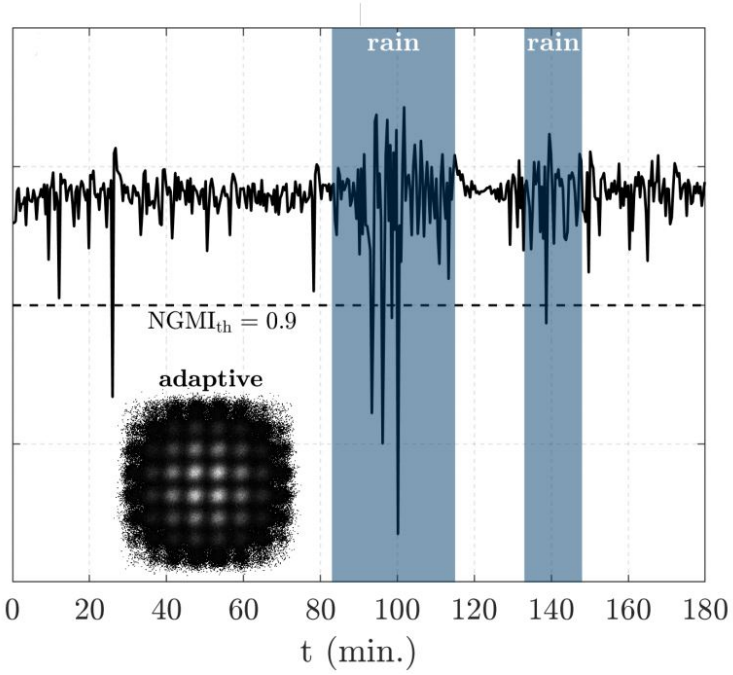

Figure 4.5: NGMI when adaptive PCS is applied

using the adaptive PCS scheme with respect to the fixed bit-rate cases, more then 80 and 50 terabyte increase in total transferred information is achieved over 3 hour transmission with 400 Gbit/s and 500 Gbit/s fixed modulation respectively. Rain periods also suggest that for constant rain the gain might be increased as disruption happens more frequently with the fixed 500 Gbit/s modulation.

4.3 Conclusions

FSO can be applied to many fields, as referenced throughout this document. This versatility allows for the definition of two types of situations in which this communication tool can be useful,

- High reliability
- High throughput.

In order to categorize the algorithm suitability, four characteristics are evaluated: mean capacity, accumulated capacity, number of disconnections and mean NGMI. Mean NGMI translates how optimized the connection is in terms of transmission rate; in a perfect scenario with PCS it should be as close to NGMIth as possible, however, such condition is hardly achievable in a link without compromising reliability. For this reason, the estimated SNR should be used with an offset to evade NGMIth violations.

The conclusions taken could be more accurate in terms of mean capacity, if re-connection packages were taken into account for example as part of overhead. In [44], the synchronization process is exploited as it can be preponderant especially in low fidelity systems. That can

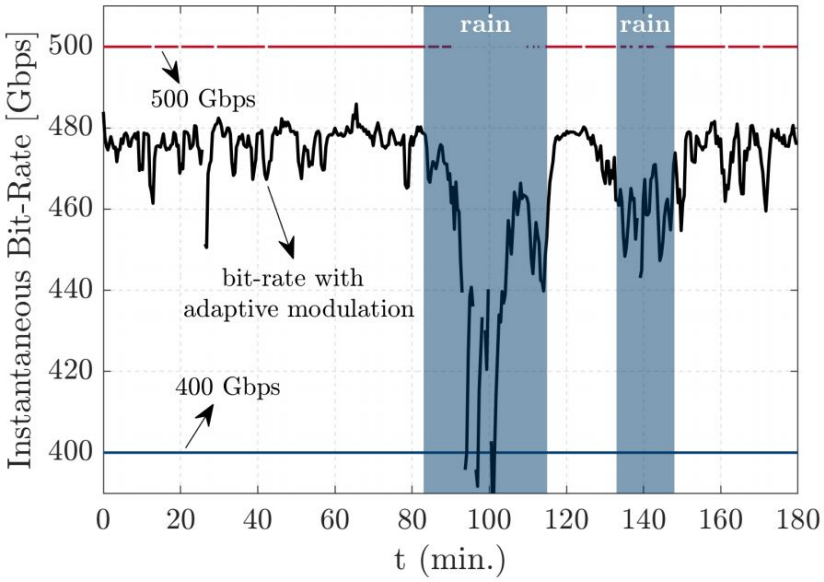

Figure 4.6: Instantaneous transmitted bit-rate with fixed and adaptive modulation

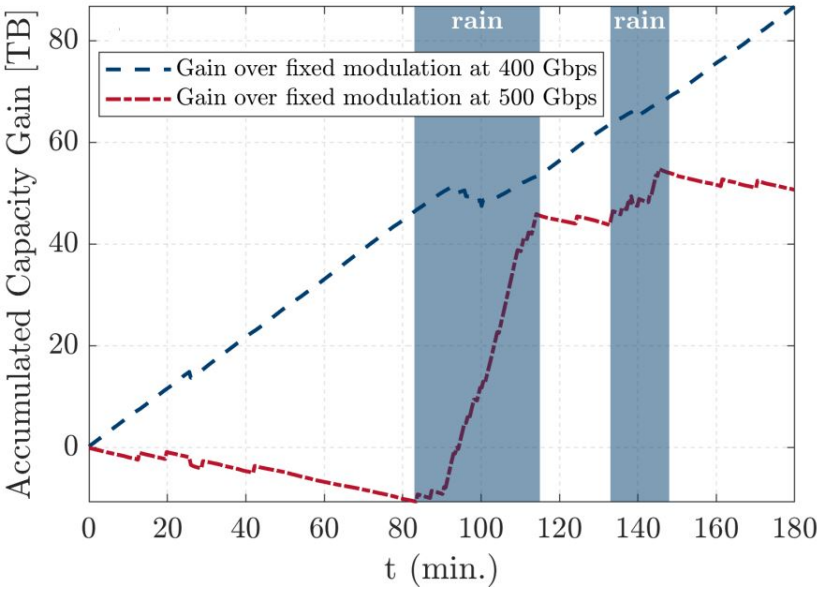

Figure 4.7: Accumulated capacity gain (in Terabytes) obtained by time-adaptive modulation over fixed modulation.

produce real transmission rates by far below the optimum transmission rate, without synchronization packages. In a generic application operating near NGMI threshold this effect should be quantified. Low reliability applications could also be empowered by correction algorithms, decreasing NGMI threshold, with the cost of increasing overhead package size.

Chapter 5

Mechanical Beam Steering

During the experiments conducted with the FSO system, the presence of several noise sources in the outdoor setup led to intensive manual alignment procedures. In fact, in the presence of windy conditions, beam misalignment error could lead to more then 3 dB losses. To correct the fade effect induced by misalignment, a mechanical beam steering system is analyzed and implemented.

5.1 Experimental Setup

The setup is composed of two colimators of the same model, with 0.017^{o} full-angle divergence and 24 mm diameter, used at transmitter and receiver end. At the end of the 27.5 m link there is a concave mirror with approximately 30 meter focal distance, being responsible for reflecting the beam from one colimator to the other. With this architecture, a 55 meter link is achieved.

At the mirror plane two Throlabs motors (models ZST206) are attached to a KM100 mirror mount, with the specifications described in Figure 5.2.

To test the described system under controlled conditions, a study was performed in a dark room with an optical bench, as depicted in Figure 5.1; this results in a link with a length of 5.5 m.

The utilized microcontroller is a low cost solution model PIC18F67J60-I/PT with maximum operation frequency of 41 MHz and it provides Ethernet connection, being useful for the feedback process. To accommodate the power over ethernet (POE) high voltages and the signal, a module is used. With this module, both communication and power feed are granted. Using a stepper motor controller, model DRV8824PWP, the motor resolution can be adjusted with increased sensibility. The micro-stepping allows to fraction the motors full step into smaller movements. The micro-stepping capability of the module allows for a maximum subdivision factor of $R_{controller} = 32$, i.e. each revolution can correspond to 32 micro-steps. The micro-stepping resolution allows only for division factors that correspond to $(2^n, 0 \leq n \leq 5, n \in \mathbb{Z})$. Motors can also be fed by a two pin connection, independent of ethernet connection. As a continuous power source, a Chemoptics TLC 13 laser is used with a maximum output power of 11 dBm operating at 1550 nm. The power is evaluated with an HP power meter, model 8153A, that connects with MATLAB, providing feedback to alignment routine responsible for mirror position optimization with 8 Hz sampling rate.

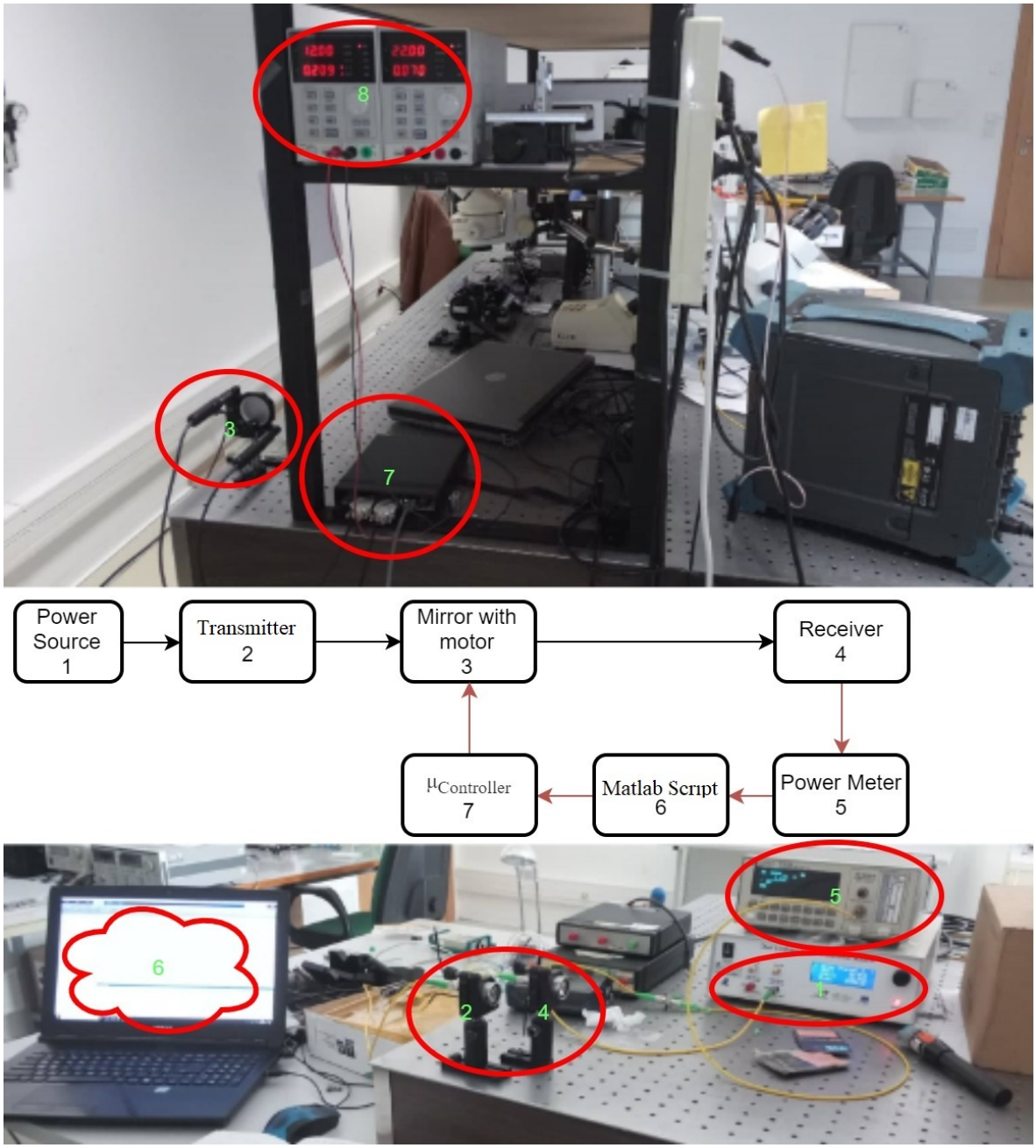

Figure 5.1: Experimental setup for indoor optimization of an automatic FSO alignment system.

5.2 Positioning System

5.2.1 Mechanical Design

For a robust positioning setup, the mechanical motion system is considered to be the only moving part, assuming both transmitter and receiver ideally static. As depicted in Figure 5.2,

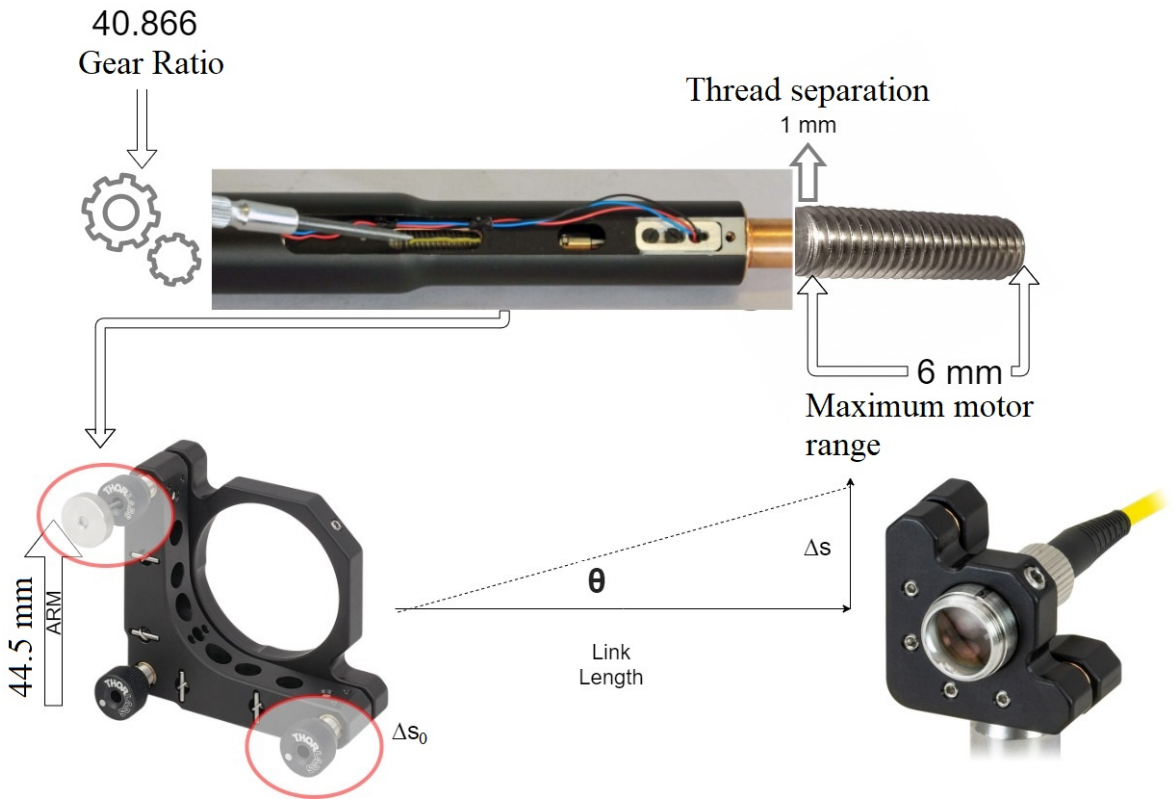

Figure 5.2: Positioning system architecture

the gear ratio (G_{ratio}) is of 40.866, as the motor output shaft performs one revolution for each 40.866 full steps, the thread separation ($T_{separation}$) is of 1 mm, therefore, the lead screw advances 1 mm for each revolution. The motor actuation is performed in each of the extremities of the kinetic mount, signaled with red contour, that are at a 44.5 mm distance (R_{arm}) of the rotation center. The minimum sensibility of the motor at the origin plan (Δs_0), corresponds to,

$$\Delta s_0 = \frac{T_{separation}}{G_{ratio} \times R_{controller}}, \tag{5.1}$$

if the controller increased resolution is not used, $R_{controller} = 1$.

Knowing the rotation arm length, the minimum traveling angle is given by,

$$\theta = arctan\left(\frac{\Delta s_0}{R_{arm}}\right) \tag{5.2}$$

The correspondent Δs_0 at the receiver plan, Δs corresponds to the same rotation angle, after

a certain link length (L_{length}),

$$\Delta s = \tan(\theta)\frac{1}{2} \times L_{length}, \tag{5.3}$$

or,

$$\Delta s = \frac{\Delta s_0 \times L_{length}}{R_{arm} \times 2 \times R_{controller}}. \tag{5.4}$$

With the properties previously listed, the system best resolution at the receiver plan without and with controller is $\Delta s = 1.5121$ mm and $\Delta s_{Controller} = 0.0472$ mm respectively.

5.3 Beam Characterization

From the mechanical characterization, it was noticeable that the system has high resolution and can be digitally controlled during alignment operations. Under outdoor conditions, beam power distribution is evaluated, using a MATLAB function to describe several expanding trajectories with square shape. The beam distribution is characterized up to a point in which connection would be considered lost (-50 dB). Horizontal and vertical motor movement are described in Figure 5.3, that displays the resulting positions occupied during the experience. Power distribution characterizes the system, since it provides the maximum displacement for

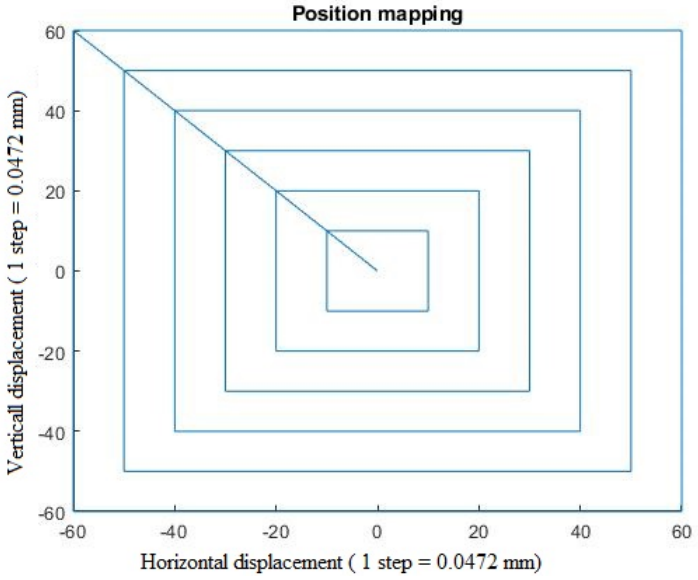

Figure 5.3: Trajectory definition for the two stepper motors (horizontal and vertical axes) in order to characterize the impact of pointing errors on the received optical power (see Figure 5.4).

which there is still connection. Defining the maximum attenuation also defines the beam width and therefore the resolution for the positioning system. Power distribution shows that for a maximum allowed attenuation, there can be an approximated maximum displacement.

First measurements revealed that high frequency variations were present, to reduce their impact averaging was performed for each position with 100 samples. The power with respect

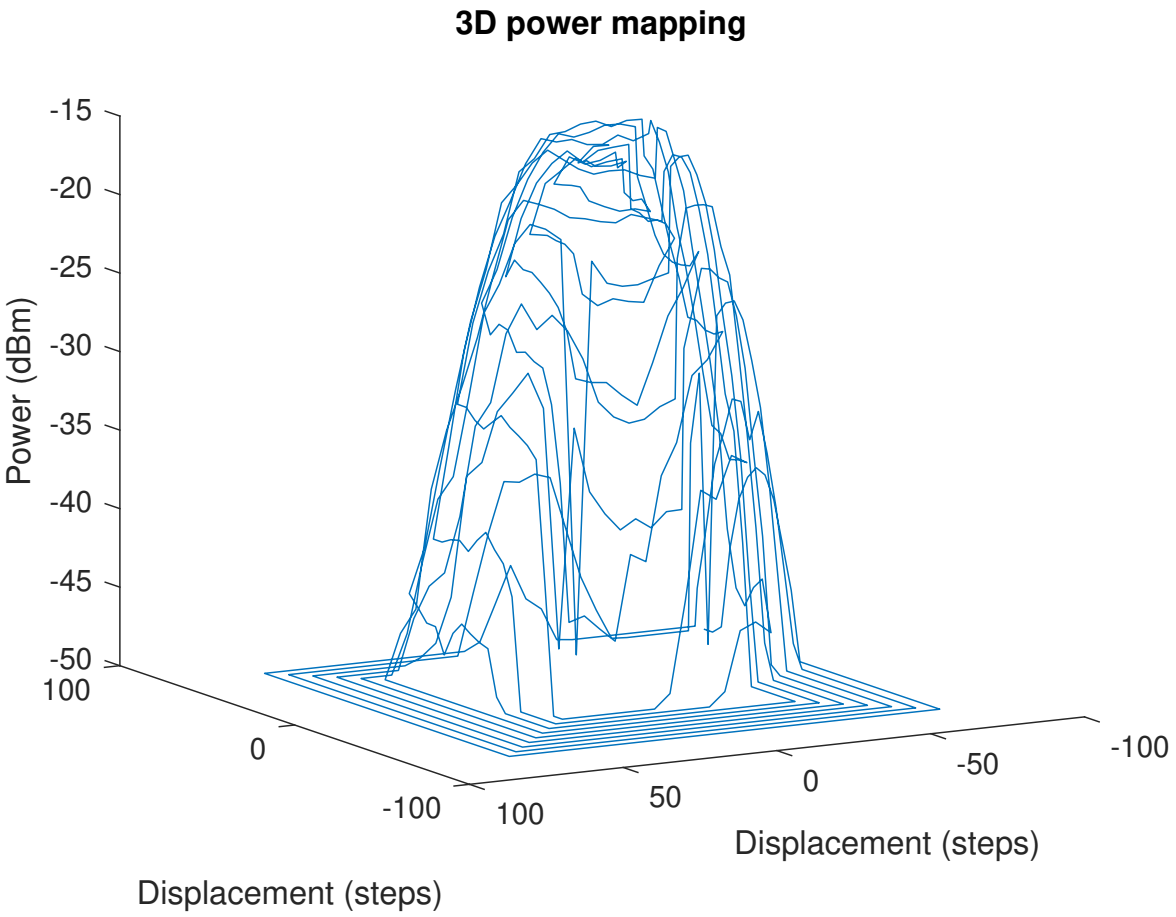

Figure 5.4: Power Distribution as a function of displacement

to each direction displacement is shown in Figure 5.4. The channel power distribution behaves similarly to a Gaussian curve, therefore the optimum alignment needs high precision as evidenced in the Figure 5.4. The allignment is optimized by maximizing the power for the specific link conditions, defining the optimal power ($P_{optimal}$) and it results from the approximation that the power changes similarly for vertical and horizontal displacements. When significant attenuation with respect to the optimized power impacts the channel, there can be an estimation process that allows to associate it to a determined positional displacement. Such approach assumes that variations are mainly due to dis-positioning phenomena. The curve shown in Figure 5.5 depicts the information contained in a LUT, that explores the beam characterization to predict the alignment correction needed. The curve is extracted by optimizing the position with respect to one axis and then changing the other one, leading to an one dimension characterization.

5.4 Proceeding for the Motor Alignment

In a situation of beam misalignment, the communication can be impaired or even disabled. For high debit communications, every second represents a lot of information, therefore the

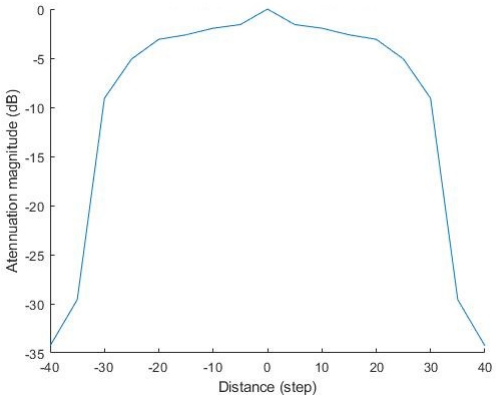

Figure 5.5: Attenuation as a function of displacement

positional error correction needs to be fast. The motors are attached to the mirror stand, assuming movement stability for both transmitter and receiver. Reducing the number of search points is a high priority, especially when the beam power is highly concentrated. Due to the existence of local minimum, there is the need to monitor the power of the control signal and mantain it within certain boundaries that allow a reliable transmission. To restrain the number of search points, a three stage approach is tested as Figure 5.6 suggests. The first

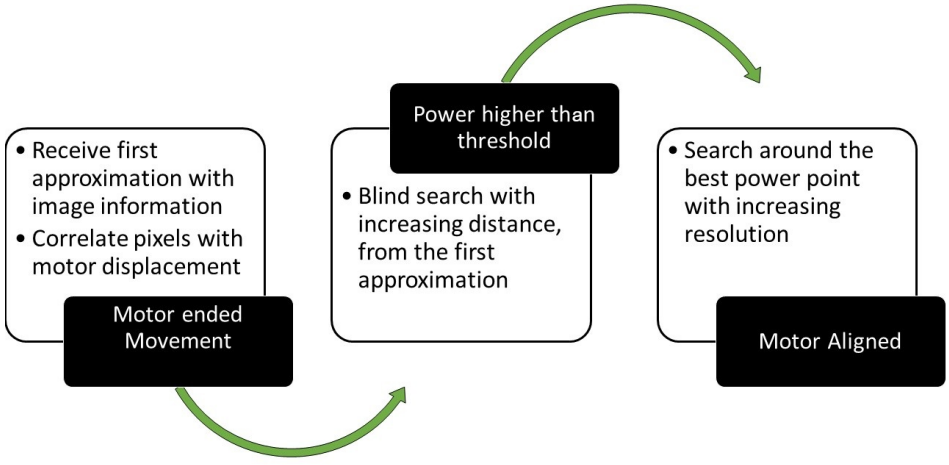

Figure 5.6: Block diagram of the proposed 3-staged FSO alignment scheme.

stage is typically executed after deploying all the hardware to achieve minimum alignment. Despite using manual allignment as a first approach, it is recommendable the exploitation of other methods (e.g. image processing to correlate pixels and motor displacement). To allow user friendly motor regulation an application is developed within app designer environment embed in MATLAB. Figure 5.7 shows the graphic user interface that allows simple directional commands to be sent to the motor, as well as to use an automatic allignment algorithm. To perform simple movements of motor, the step size and micro step resolution can be adjusted as

intended. The field "number of samples" allows power measurement to be averaged, filtering high frequency components, an important tool in outdoor systems with high variance.

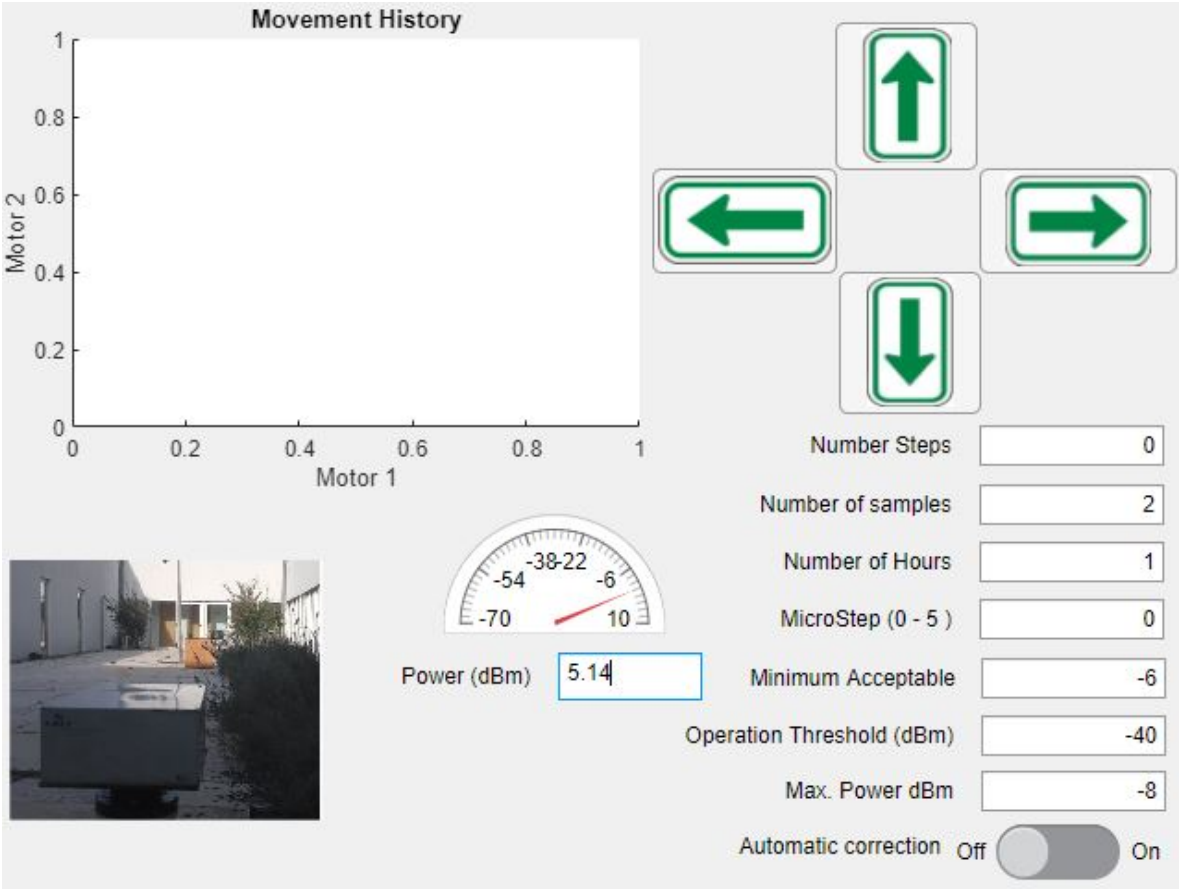

Figure 5.7: MATLAB-based application interface for automatic FSO alignment.

5.4.1 Blind Search

This method is the one with the lowest complexity and is used because in general the system can not acquire information in this phase, to feed a non-linear algorithm e.g. Gradient descent or Nelder-Mead simplex. The method proposes that from the beam characterization, maximum resolution can be set to reduce the number of points to evaluate. Now that the resolution is defined and that trajectory is as presented in Figure 5.3, a stop condition needs to be defined. The stop condition is dependable on the power detection resolution, therefore, reduced sensibility is assumed ($P_{threshold} = -50$ dBm) assuring that system can be used for all power meters available in the laboratory of Instituto de Telecomunicações, for the specified wavelength. Once a power level greater then $P_{threshold}$ is detected by the algorythm, the control flux enters into higher precision stage, i.e. the fine tuning phase.

5.4.2 Fine Tuning

Once a minimum power is acquired, the algorithm enters the high precision stage, optimizing the steering system resolution. This proceeding is characterized by higher precision movement. To produce fast convergence the system uses a non-linear control method to search for the best position, based on the gradien descent algorithm.

Gradient Descent

This approach is more likely to converge, if the adjustment precision is higher. However, it might sacrifice convergence time as it tests, for every iteration, what is the best neighbour point, creating a total of 8 point constellation, at each iteration. As illustrated in Figure 5.8, once one solution performs better then the remaining, the algorithm iterates towards its

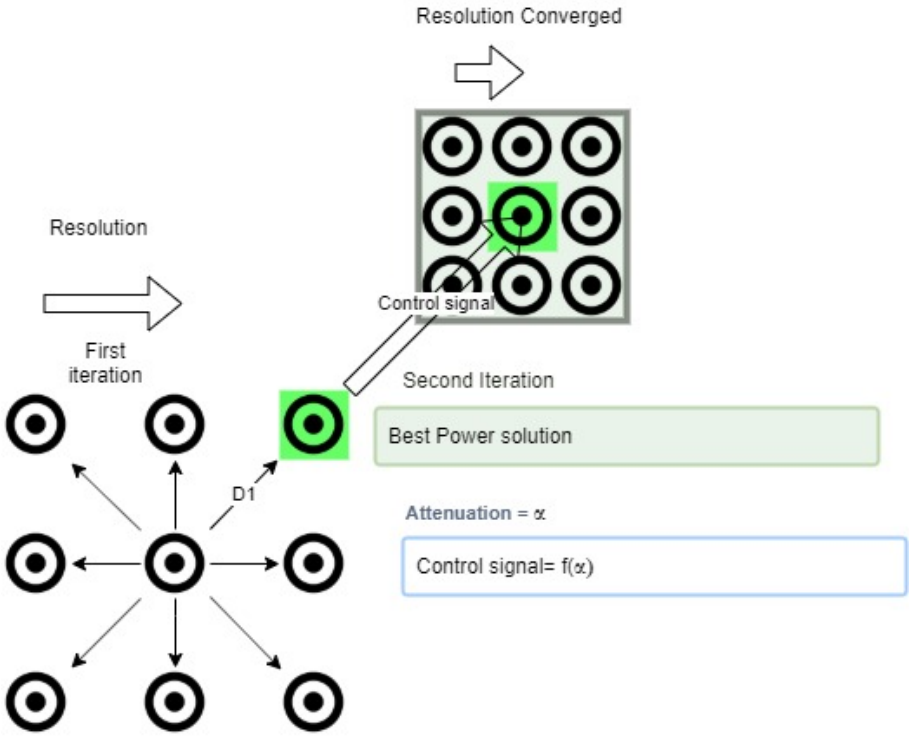

Figure 5.8: Algorithm flow

direction, e.g (D1). In the gradient descent, the step magnitude is typically defined as a function of the derivative or second derivative of the error function, in this case, the attenuation function [45]. However, with reduced computing requirements and making use of information obtained from beam characterization, the control signal (C_{signal}) quantization is made as a function of the attenuation, using the information contained in Figure 5.5.

$$C_{signal} = f(\alpha) \times k_p \tag{5.5}$$

In the experiments, the proportional gain is set as $k_p = 0.8$, preventing motor from over-compensating and inducing control signal oscillation. Once no neighbour point has improved

power when compared to a previous solution, the algorithm enters a sleep mode until the power experiences two or more dB attenuation with respect to the new solution. This represents a compromise to avoid the motor being activated to compensate power fluctuations from other sources of error non-related with positioning e.g. due to atmospheric turbulence.

5.5 Indoor Automatic Alignment

The manual steering system presented some deviations over the experiments, contributing to power losses, consequently degrading the SNR. To improve power budget optimization, the gradient descent algorithm is applied with four distinct variants,

- Fixed step correction;
- Proportional integral derivative (PID);
- Adaptive correction based on beam characterization;
- Adaptive correction based on derivative of beam attenuation;

as described in Section 5.4.2, where the control signal is set accordingly to the variant used.

Under laboratory conditions the received power variance is within 0.02dB and therefore it allows the experiments to be carried out under controlled conditions. As a consequence of channel stability, all the losses are considered fixed. Because the attenuation caused by natural misalignment of the system is almost negligible, there is not enough noise to test the positioning system.

With a Matlab routine, equally distributed positioning perturbations are induced, creating attenuation that emulates outdoor impairments typical in a long term outdoor communication. A perturbation of the control signal is generated periodically, as displayed in Figure 5.9. The maximum induced distortion is limited by 2.5204 mm in each axis, as explicit in the Figure 5.4. Such limitation is executed with a controller sub-scale of $R_{controller} = 4$, in a 5.5 m link length.

5.5.1 Fixed Step Correction

In order to evaluate motor functionalities, as well as algorithm behaviour, a simple approach is Proposed. By setting fixed correction resolution of 0.630 mm, the power is sampled at 8 Hz and after averaging over 10 consecutive samples, a perturbation signal is injected, as depicted in Figure 5.9. The algorithm is set to use gradient descent, once the power drops bellow a certain threshold from the optimum power. If the minimum acceptable level is reached, the adjustment stops; this approach releases the motor from stress, reducing drastically the actuation number. However, as Figure 5.10 shows, frequently power levels stay below optimum power, not optimizing link conditions to the maximum. In this figure, red points represent the moment when a perturbation is injected into channel; when the received power is below the -2 dBm threshold, the motor performs trajectory correction. Results show that this methodology allows for high power variations. The disconnection time is already a good indicator, proving that the motor can produce trajectory correction. Nevertheless, in some cases the threshold is not reached before other perturbations impact the link. To overcome problems that remain with the usage of this algorithm, adaptive resolution correction techniques are experimented.

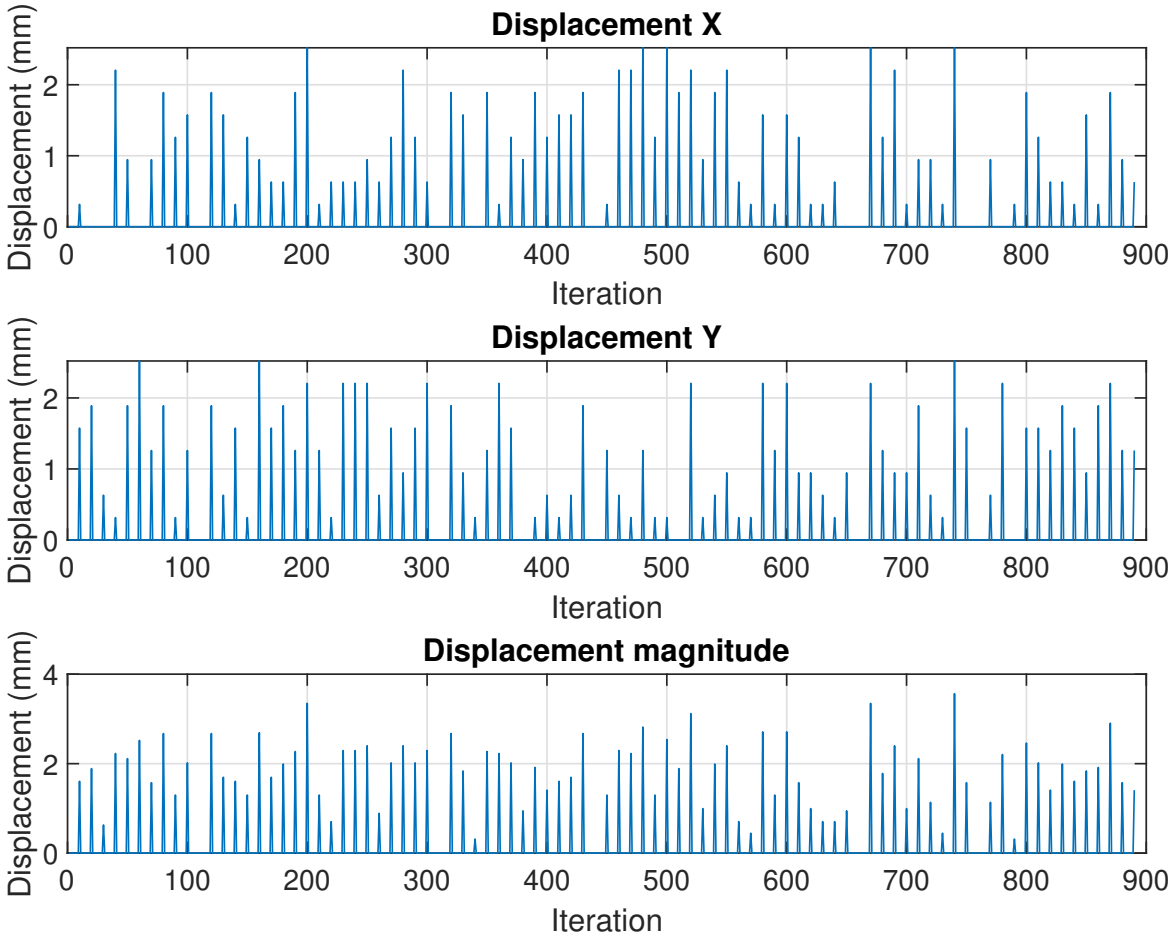

Figure 5.9: Induced perturbation - Fixed step correction perturbation vectors

5.5.2 Proportional Integral Derivative (PID)

With this controller, the motor movement is computed as,

$$u(t) = k_p e(t) + k_i \int_0^t e(\tau)d\tau + k_d \frac{de}{dt} \tag{5.6}$$

, where k_p, k_i and k_d are the proportional, integral and derivative constants, respectively and the $e(t)$ that corresponds to the attenuation with respect to the optimum position. To tune the PID constants, the Ziegler-Nichols method can be used, as in [46]. However, due to motor backlash, and the difficulty to address the system dead time with the power sampling rate available, the constant tuning process is made through experimentation. The results are depicted in Figure 5.11.

A conservative 0 dBm threshold is considered, avoiding excessive motor activation. Furthermore, to reduce the rise-time, k_i was increased, leading to higher attenuation stages in correction process. Nevertheless, the convergence time is generally met between two imposed perturbations. As overshoot is present with this combination of coefficients, there is the need for a different algorithm to produce a more constrained behaviour, with lower margin between optimum attenuation and the acceptable one.

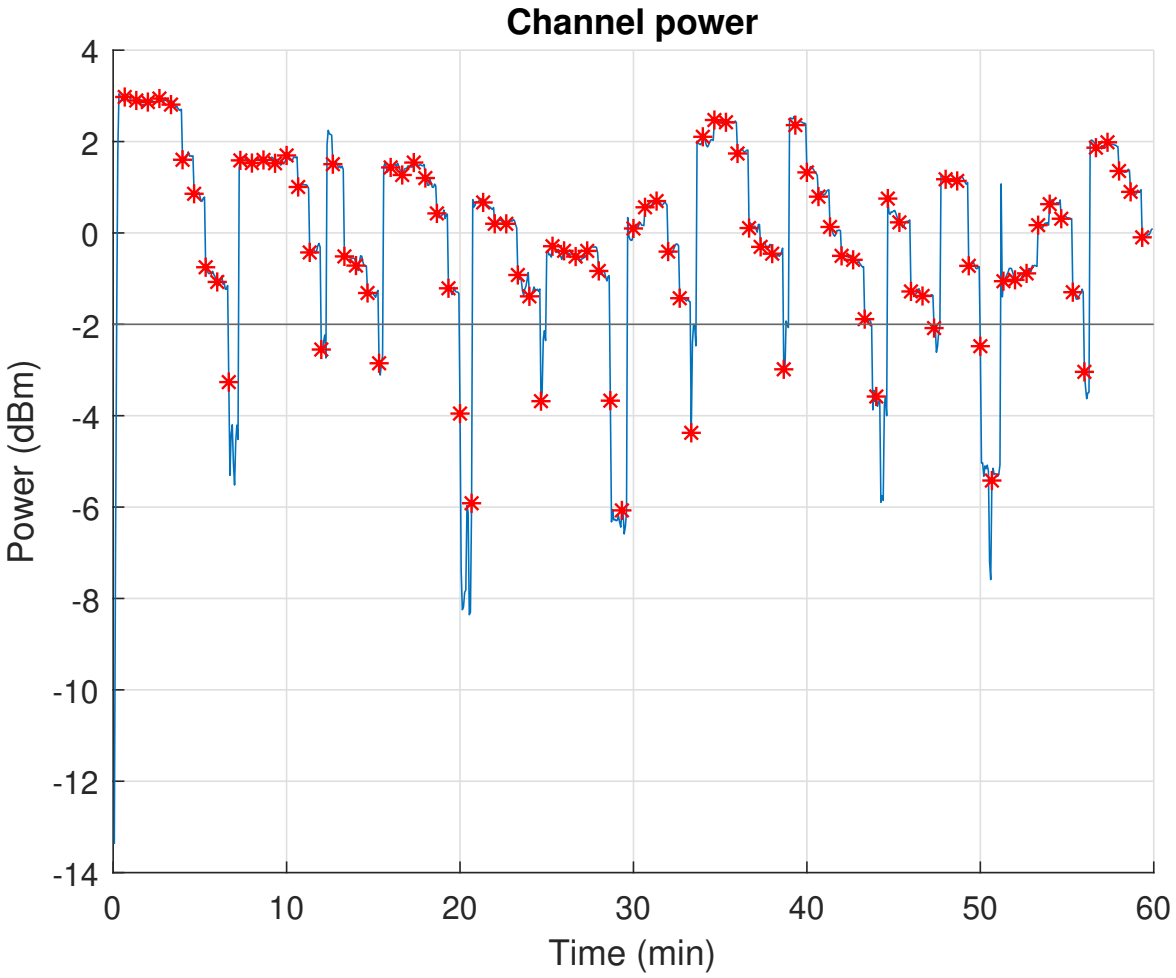

Figure 5.10: Received optical power over time with periodically random induction of pointing errors (red markers) and respective compensation through automatic alignment using fixed step correction (blue solid line).

5.5.3 Adaptive Correction Based on Beam Characterization

The fixed step correction algorithm presents some characteristics that need to be improved, like variance and, in some occasions, alignment was not reached within reasonable time. To overcome these problems, instead of using a completely blind algorithm, information from beam profiling is used to construct a LUT that for a given attenuation provides correction amplitude to achieve an estimated optimum point. In this experiment, a dump factor of 0.88 is considered, Figure 5.12 displays the channel behaviour under these circumstances. The average power is higher than previously, and the variations are also smaller, however, the stabilized power is still far below the maximum one in most cases. Another good indicator that this algorithm can be adjusted based on LUT is the fact that, with reduced number of iterations, the power reaches the threshold level. To raise the threshold to a higher value, position adjustment was implemented in two stages, making use of the previous LUT in both of them. Second stage starts when the power reaches 1.5 dBm, refining the position with higher

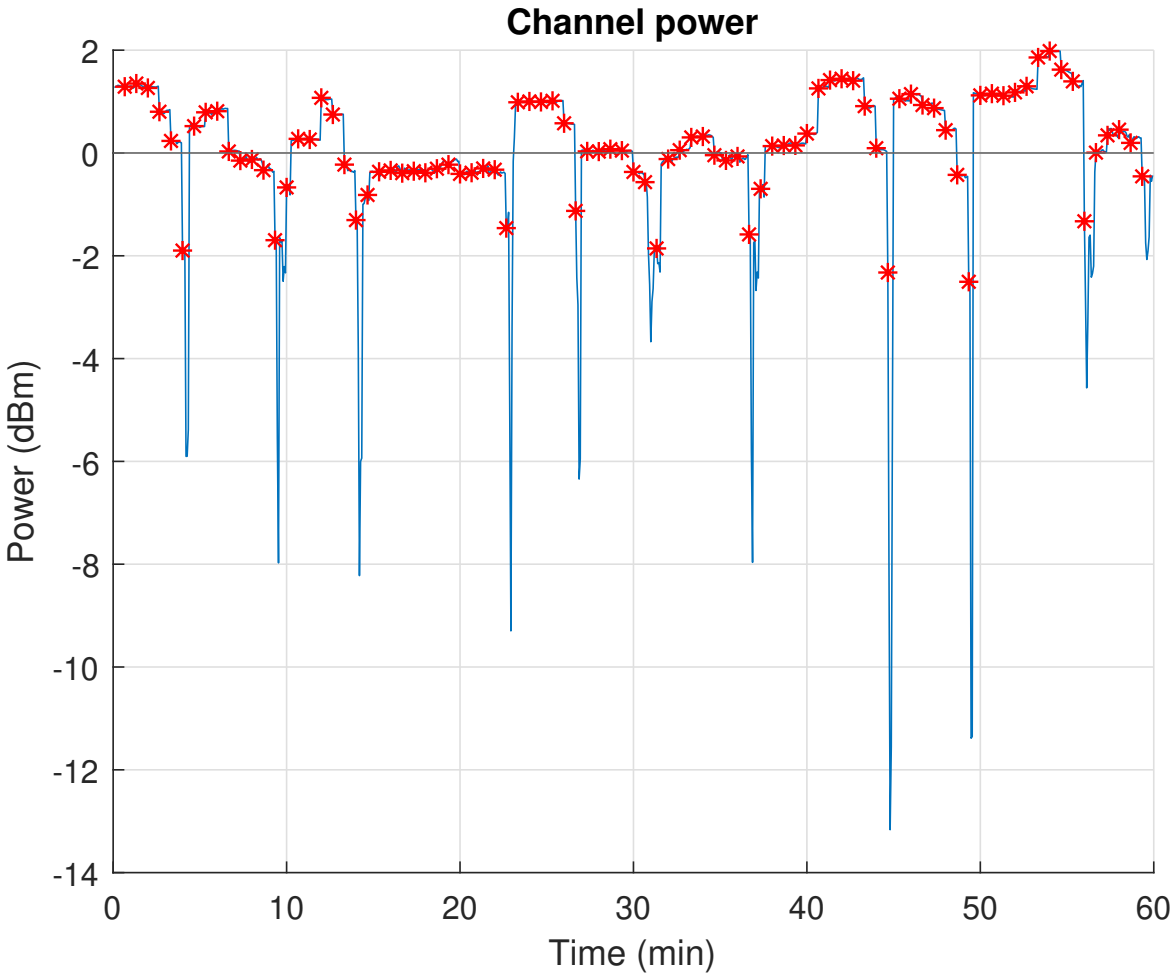

Figure 5.11: Received optical power over time with periodically random induction of pointing errors (red markers) and respective compensation through automatic alignment using the PID algorithm of expression(5.6) (blue solid line).

---

resolution, which is achieved by setting $R_{Controller} = 4$. Such precision is not used in the first stage to promote faster functioning of the motor. With the second stage, higher precision is achieved as exhibited in Figure 5.13. In this process, the mean value is highly increased, and the perturbations have minimal cumulative effect. Therefore the signal excursion is reduced. The link variance is reduced and threshold value violations as well, even though the threshold value is higher. As fine tunning corrections could be slower, the perturbations were injected with approximately 3 min interval.

5.6 Conclusions

After successfully the automatic FSO alignment procedure the performance of the experiments is evaluated with the metrics presented in Table 5.6. For four distinct control signal calculation algorithms the following parameter are analysed: average power; average convergence time; number of disruptions (passages of power bellow threshold), maximum convergence

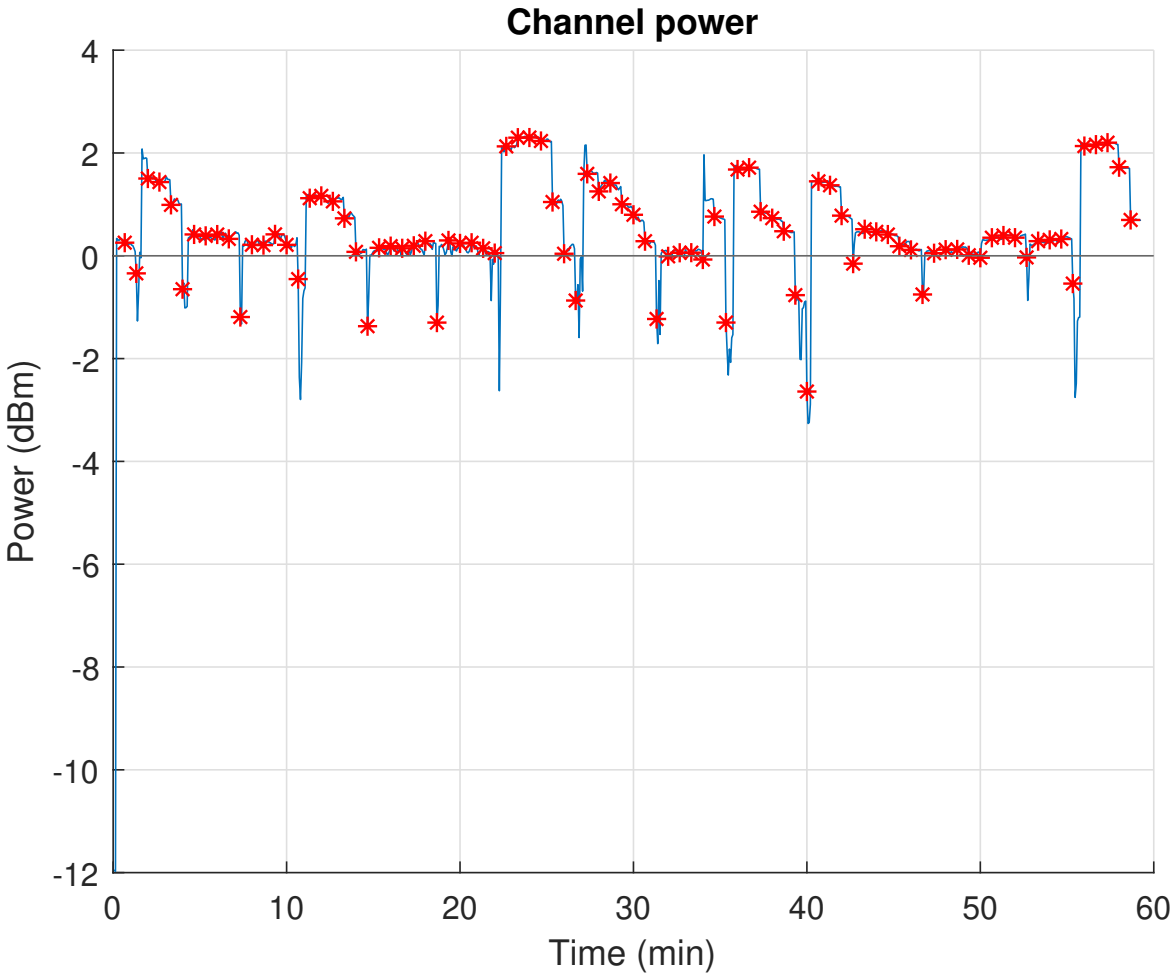

Figure 5.12: Received optical power over time with periodically random induction of pointing errors (red markers) and respective compensation through automatic alignment using the LUT-aided adaptive correction algorithm (blue solid line).

---

time, activation threshold and perturbation period imposed.

Fixed correction presents higher variance as well as lower average power. Convergence speed is reduced but it is contained within a -2 dBm power threshold, not being satisfactory for the majority of applications as it would correspond to 4 dB attenuation motivated only by misalignment. The maximum convergence time is higher than the perturbation period indicating that the algorithm was not able to perform correction.

Using the PID to compute the adaptive control signal provides better results correction step algorithm, as expected. Therefore the threshold level was increased to 0 dbm, accepting 2 dB attenuation. The variance is approximately half of the one experienced with the fixed alternative, the average power increased by a residual value, as consequence of high average convergence time. From such information it is clear that an informed criterion should be used to produce the control signal.

Using the LUT containing information extracted from beam characterization leads to better results than previous alternatives. Average power and variance outperform other techniques

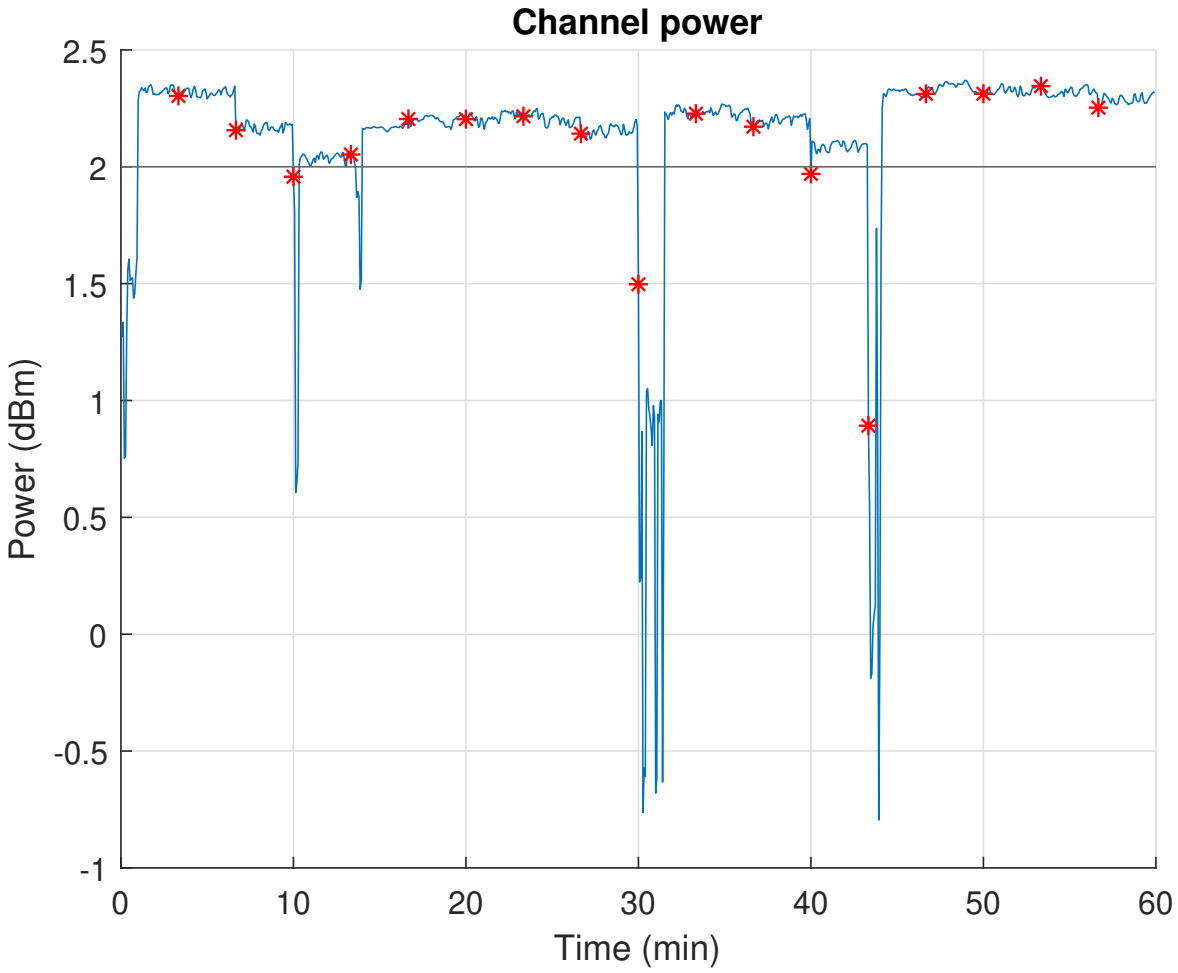

Figure 5.13: Received optical power over time with periodically random induction of pointing errors (red markers) and respective compensation through automatic alignment using a dual-state LUT-aided adaptive correction algorithm (blue solid line).

presented. The induced perturbations show that the system was led to disruption several times and still recovered in most of the occasions in the time interval expected. In fact, the average number of iterations to produce power within expected the level is near 1, meaning that the system convergence is almost immediate. The maximum number of corrections needed to achieve the minimum power threshold of 0 dBm taking 1 min. From the results obtained with LUT information, we conclude that the correction ability is still not being used at its full potential. To implement finer correction, two LUTs are used: the same in all regions below 2 dBm and another with motor $R_{controller} = 8$ doubling motor precision and $k_p = 0.5$, thus highly reducing the control signal excursion. The obtained results show that a higher quality of alignment is obtained, the average power highly increased, the convergence time is acceptable and the number of disruptions induced by the perturbation signal is reduced, even though, the threshold level is closer to the optimum power, in comparison to the other methods. The channel is more robust and shows that if an active control system is used then the ability to mantain it stable and independent of misalignment is higher.

Control	Average power (dBm)	Average Convergence Time (s)	Number of Disruptions	Maximum Convergence Time (s)	Power Threshold (dBm)	Perturbation Period (s)
Fixed-step	0.1879	24	15	85	-2	40
PID	0.2044	136	10	730	0	40
LUT	0.5984	6	27	60	0	40
Dual-stage LUT	2.1444	30	6	110	2	200

Table 5.1: Positioning algorithms overview

Chapter 6

Conclusions and Future Work

6.1 Conclusions

This thesis was conceived with the objective of producing further analysis of FSO technology, being a topic of interest in the scope of low-cost high-capacity communication systems, for medium and short range applications. This type of communication can be highly dependent of the atmospheric interactions, therefore, a further study of several destructive phenomenon was conducted.

FSO communication links are prone to several types of distortion, leading to a time varying link. To track such variations, several link loss modeling algorithms were implemented and tested, providing an highly accurate channel estimation for different weather conditions.

To overcome the channel variance and to optimize the transmission, the concept of probabilistic constellation shaping was utilized in order to enable an efficient bit-rate adaptation to the current FSO link conditions. The adaptive transmission rate was adjusted accordingly with the information extracted from the estimation algorithms. For a 3 hour transmission impaired with rain, an accumulated capacity gain of more than 50 Terabytes has been demonstrated by applying this time-adaptive channel estimation and modulation technique.

For long-term experiments the communication link experienced persistent attenuation that could lead to more then 3 dB losses. By using the manual beam steering gimbal the attenuation could be compensated, evidencing that the main source of the losses was due to positioning error. Using two motors to perform the correction, several automatic allignment alternatives were tested, enabling to significantly reduce the overall link loss induced by pointing errors.

6.2 Future Work

6.2.1 Free Space Optics Weather Modeling

The Instituto de Telecomunicações in Aveiro has a weather monitoring station within the campus, allowing for weather condition tracking. With the data that can be extracted from the weather station, the system modelling can explored. Real time weather monitoring from the server was already implemented. However, the refresh rate of the server that provides sensor measurements only refreshes every 15 minutes.

6.2.2 Implement an Hybrid FSO and VLC System

FSO systems are typically associated to inter building communications. However, the signal still needs to be distributed withing the building. To achieve signal dissemination, VLC system can be used as shown in Figure 6.1.

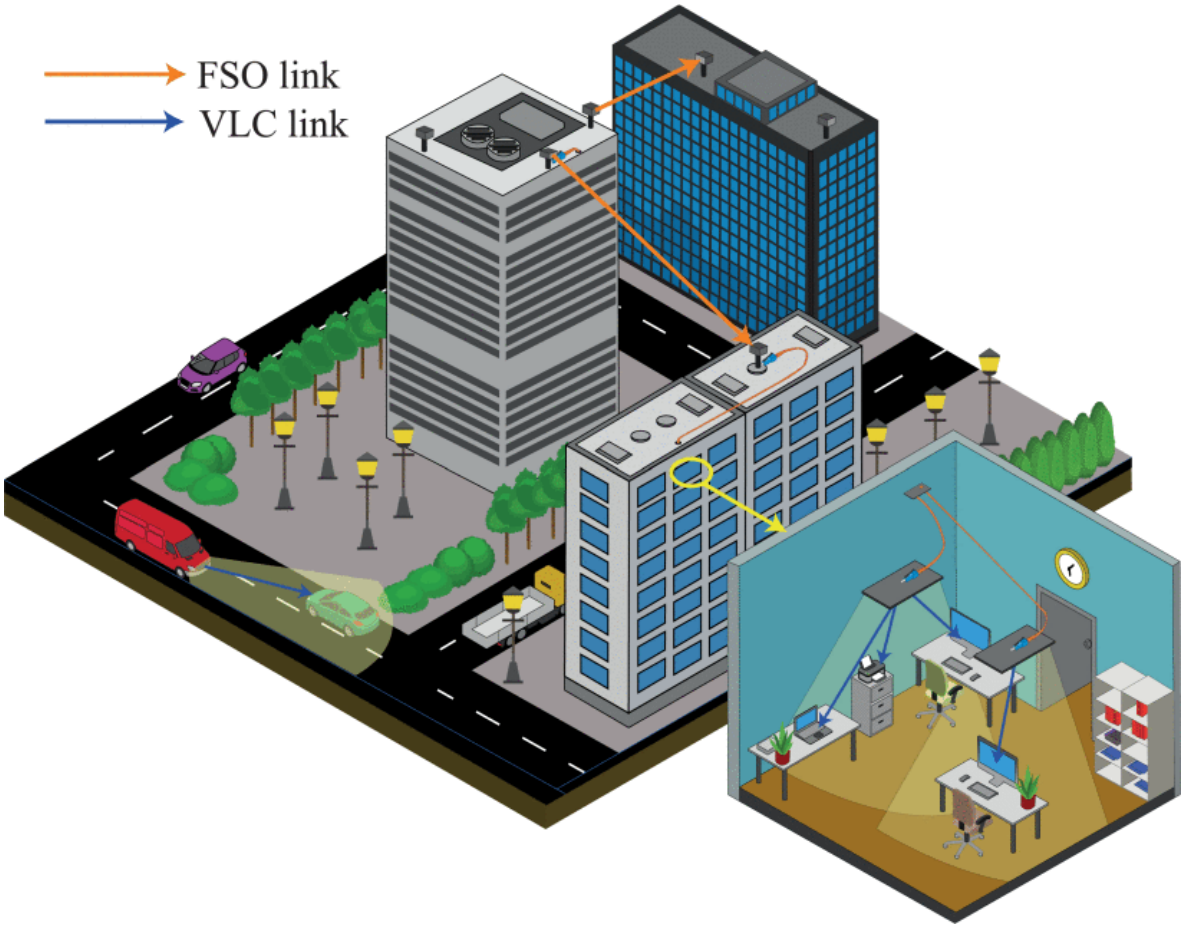

Figure 6.1: Last mile access with FSO and VLC [47]

6.2.3 FSO Wireless Power Transmission (WPT)

WPT is becoming highly popular as it can be used for simpler activities, as charging small peripherals to the point of powering electrical cars and unmanned planes. Figure 6.2 shows an overview of WPT methods, laser power transmission has high directivity and therefore it can be posed as long distance alternative, the main limitation is the tracking mechanism.

6.2.4 Underwater Communications

Underwater optical wireless communications (UOWC) has been subject of study in the last years. The acoustic underwater communication is highly usual, however, it's low data-rates are a limitation when the intention is to investigate climate change e.g.: unmanned underwater vehicles (UUVs) can be used for oil production refineries. Therefore there is an

WPT technologies		Strengths	Weaknesses	Example applications
Inductive Coupling		Simple, high power transfer efficiency in centimeter range	Short charging distance, requiring accurate alignment in charging direction	Electric toothbrush, charging pad for cell phones and laptops
EM radiation	Omnidirectional	Tiny receiver size	Rapid drop of power transfer efficiency over distance, ultra low-power reception	Charging a WSN for environmental monitoring (temperature, moisture, light, etc.)
	Unidirectional (microwave/ laser)	Effective power transmission over long distance (kilometer-range)	Requiring LOS and complicated tracking mechanisms, inherently large scale of devices	SHARP unmanned plane
Magnetic resonant coupling		High efficiency over several meters under omni-direction, not requiring LOS, and insensitive to weather conditions	High efficiency only within several-meter range	Charging mobile devices, electric vehicles, implantable devices and WSNs

Figure 6.2: Wireless power transfer technologies [48]

interest in exploiting higher capacity underwater communications. It is also important to grant reliability. Therefore, there is also an interest on using retro-reflector mirrors to expand LOS [49].

Underwater communication can achieve 2.7 Gbp/s with a green laser diode and NRZ-OOK modulation over a 34.5m link [50]. Figure 6.3 shows the water absorption spectrum. There is a clear attenuation increase in the 1550 nm band when compared to visible communication spectrum. That motivates the exploitation of underwater communications at lower wavelengths.

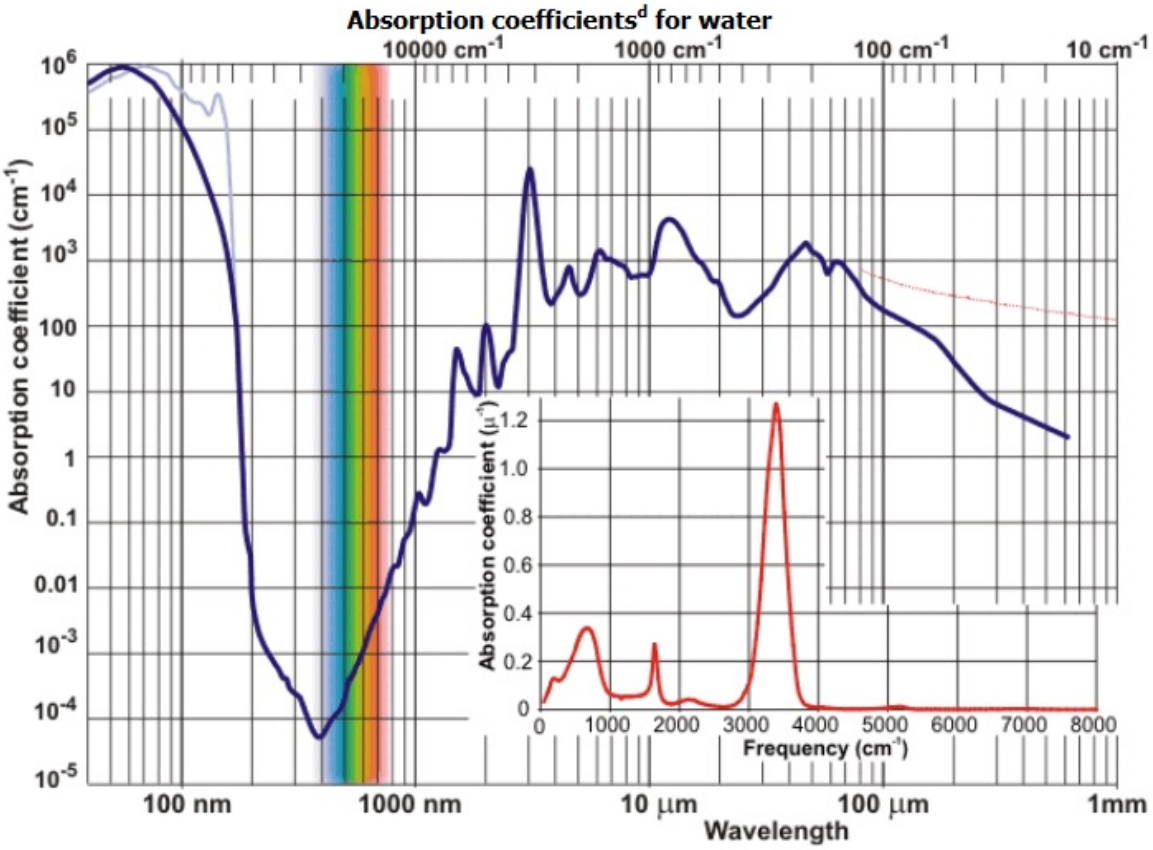

Figure 6.3: Water absorption spectrum [51]

References

[1] M. Andrew. Bandwidth Demand In Student Housing. `http://www.bbpmag.com/Features/1012feature.php`. Accessed: 2019-09-25.

[2] Yiqiao Wei and Seung-Hoon Hwang. Investigation of spectrum values in rural environments. *ICT Express*, (vol. 4):pages 234–238, dec 2018.

[3] Aditi Malik and Preeti Singh. Free Space Optics: Current Applications and Future Challenges. *International Journal of Optics*, pages 1–7, nov 2015.

[4] M. Ijaz, Z. Ghassemlooy, J. Pesek, O. Fiser, H. Le Minh, and E. Bentley. Modeling of Fog and Smoke Attenuation in Free Space Optical Communications Link Under Controlled Laboratory Conditions. *Journal of Lightwave Technology*, vol. 31:pages 1720–1726, jun 2013.

[5] Suriza Ahmad Zabidi, Wajdi Al Khateeb, Md. Rafiqul Islam, and A. W. Naji. The effect of weather on free space optics communication (FSO) under tropical weather conditions and a proposed setup for measurement. In *International Conference on Computer and Communication Engineering (ICCCE'10)*, pages 1–5. IEEE, may 2010.

[6] IEC Standard - Home. `https://webstore.iec.ch/publication/3587`. Acessed 2019-08-26.

[7] K. Yoshida, Kuniaki Tanaka, Kazunori Katayama, T. Tsujimura, and Yuji Azuma. Collimator focus adjustment for free space optics system using single-mode optical fibers. In *2009 ICCAS-SICE*, pages 1338–1341, Aug 2009.

[8] D. L. Hutt, K. J. Snell, and P. A. Bélanger. Alexander graham bell's photophone. *Opt. Photon. News*, vol. 4:pages 20–25, Jun 1993.

[9] A G Bell. The photophone. *Science (New York, N.Y.)*, vol. 1, Sep 1880.

[10] Silvanus P. Thompson. The Photophone. *Nature*, 22(569):481–481, Sep 1880.

[11] Christopher H. Sterling. *Military communications : from ancient times to the 21st century*. ABC-CLIO, 2008.

[12] Samridhi Wazir. Capstone project report-"Data And Voice Communication Using Laser". Technical report, Lovely Professional University, Phagwara, 2014.

[13] EC SYSTEM. Case studies of deployment wireless equipment. `http://www.ecsystem.cz/en/case-studies`, 2019. Accessed 2019-10-26.

[14] Free Space Optics (FSO) worth $1.45 billion and Visible Light Communication (VLC)/Light Fidelity (Li-Fi) Market worth $75.00 billion by 2023. https://www.marketsandmarkets.com/PressReleases/visible-light-communication.asp. Accessed 2019-08-27.

[15] Building an ook system. https://electronics.stackexchange.com/questions/25682/ook-system-question. Accessed: 2019-09-25.

[16] Amplitude shift keying. https://www.open.edu/openlearn/science-maths-technology/exploring-communications-technology/content-section-1.4. Accessed: 2019-09-25.

[17] Bobby Barua. Comparison the performance of free-space optical communication with ook and bpsk modulation under atmospheric turbulence. *International Journal of Engineering Science and Technology (IJEST)*, vol. 3:pages 4391–4399, 2011.

[18] Quadrature phase shift keying. https://www.allaboutcircuits.com/technical-articles/differential-quadrature-phase-shift-keying-dqpsk-modulation/. Accessed: 2019-09-27.

[19] Joseph M Kahn. Modulation and Detection Techniques for Optical Communication Systems. Technical report, Stanford University, California, 2006.

[20] Wi-charge - Power without Wires. https://www.wi-charge.com/products-overview/. Accessed: 2019-02-20.

[21] D. Young J. Juarez A. Dwivedi N. Demidovich III J. Graves M. Northcott J. Douglass J. Phillips R. Sova, J. Sluz. *80 Gb/s freespace optical communication demonstration between an aerostat and a ground terminal*. SPIE, 2006.

[22] Pei-Lin Chen, Shenq-Tsong Chang, Shuen-Te Ji, Shu-Chuan Lin, Han-Hsuan Lin, Ho-Lin Tsay, Po-Hsuan Huang, Wei-Chieh Chiang, Wei-Cheng Lin, San-Liang Lee, Hen-Wai Tsao, Jin-Pu Wu, and Jingshown Wu. Demonstration of 16 channels 10 gb/s wdm free space transmission over 2.16 km. In *2008 Digest of the IEEE/LEOS Summer Topical Meetings*, pages 235–236, July 2008.

[23] Ernesto Ciaramella, Yoshinori Arimoto, Giampiero Contestabile, Marco Presi, Antonio , D'Errico, Vincenzo Guarino, and Mitsuji Matsumoto. 1.28 Terabit/s (32x40 Gbit/s) WDM Transmission over a Double-Pass Free Space Optical Link. *Optical Fiber Communication Conference and National Fiber Optic Engineers Conference*, 2009.

[24] Arun K. Majumdar. *Optical wireless communications for broadband global internet connectivity : fundamentals and potential applications*. Elsevier, 2018.

[25] Mohammad Ali Khalighi and Murat Uysal. Survey on Free Space Optical Communication: A Communication Theory Perspective. *IEEE Communications Surveys & Tutorials*, vol. 16:pages 2231–2258, 2014.

[26] Climate Change and Climate Modeling, Cambridge UP. http://slideplayer.com/slide/5076155/. Accessed: 2019-09-27.

[27] Jasjot Kaur Sahota and Divya Dhawan. Reducing the effect of scintillation in FSO system using coherent based homodyne detection. *Optik*, vol. 171:pages 20–26, oct 2018.

[28] Ales Prokes. Modeling of atmospheric turbulence effect on terrestrial fso link. *Radioengineering*, 18, April 2009.

[29] S. Sheikh Muhammad, P. Köhldorfer, and E. Leitgeb. Channel modeling for terrestrial free space optical links. In *Proceedings of 2005 7th International Conference on Transparent Optical Networks, ICTON 2005*, volume 1, pages 407–410, 2005.

[30] Maged Abdullah Esmail and Habib Fathallah. Improved wavelength independent empirical model for fog attenuation in FSO communication systems. In *2016 7th International Conference on Information and Communication Systems, ICICS 2016*, pages 196–200. Institute of Electrical and Electronics Engineers Inc., may 2016.

[31] El dorado Weather. Europe average anual rain rate. `https://www.eldoradoweather.com/forecast/climate/climate-maps/europe-annual-precip-map.html`. Accessed: 2019-09-27.

[32] Mukesh Chandra Kestwal, Sumit Joshi, and Lalit Singh Garia. Prediction of rain attenuation and impact of rain in wave propagation at microwave frequency for tropical region (Uttarakhand, India). *International Journal of Microwave Science and Technology*, 2014.

[33] Umair Korai, Lorenzo Luini, and Roberto Nebuloni. Model for the Prediction of Rain Attenuation Affecting Free Space Optical Links. *Electronics*, vol. 7:page 407, dec 2018.

[34] M. Naruse, S. Yamamoto, and M. Ishikawa. Real-time active alignment demonstration for free-space optical interconnections. *IEEE Photonics Technology Letters*, vol. 13:pages 1257–1259, nov 2001.

[35] Free Space Optical Networking Architecture: wavelength selection for optical wireless systems. Technical report, fSONA Networks Corp, 2001.

[36] A. Teixeira, Ali Shahpari, Vitor Ribeiro, Ricardo Ferreira, Artur Sousa, Somayeh Ziaie, Jacklyn Reis, Giorgia Parca, Silvia Dibartolo, Vincenzo Attanasio, Stefano Penna, and Giorgio Tosi Beleffi. *FSO for High Capacity Optical Metro and Access Networks*, pages 511–526. Springer, 08 2016.

[37] C. Berrou, A. Glavieux, and P. Thitimajshima. Near Shannon limit error-correcting coding and decoding: Turbo-codes. 1. In *Proceedings of ICC '93 - IEEE International Conference on Communications*, volume 2, pages 1064–1070. IEEE, 1993.

[38] Dan Raphaeli and Assaf Gurevitz. Constellation shaping for pragmatic turbo-coded modulation with high spectral efficiency. In *IEEE Transactions on Communications*, volume 52, pages 341–345, mar 2004.

[39] L. Schmalen. Probabilistic constellation shaping: Challenges and opportunities for forward error correction. In *2018 Optical Fiber Communications Conference and Exposition (OFC)*, pages 1–3, March 2018.

[40] Junho Cho and Peter J. Winzer. Probabilistic Constellation Shaping for Optical Fiber Communications. volume 37, pages 1590–1607. Institute of Electrical and Electronics Engineers Inc., mar 2019.

[41] Junho Cho, Sethumadhavan Chandrasekhar, Xi Chen, Greg Raybon, and Peter J. Winzer. High spectral efficiency transmission with probabilistic shaping. *2017 European Conference on Optical Communication (ECOC)*, pages 1–3, 2017.

[42] Fernando Guiomar, Abel Lorences-Riesgo, D. Ranzal, F. Rocco, Artur Sousa, Andrea Carena, A. Teixeira, Carmo Medeiros, and Paulo Monteiro. High-capacity and rain-resilient free-space optics link enabled by time-adaptive probabilistic shaping. 07 2019.

[43] Georg Böcherer. Achievable Rates for Probabilistic Shaping. *Huawei Technologies France S.A.S.U.*, jul 2017.

[44] Ali A. Nasir, Salman Durrani, Hani Mehrpouyan, Steven D. Blostein, and Rodney A. Kennedy. Timing and carrier synchronization in wireless communication systems: a survey and classification of research in the last 5 years, dec 2016.

[45] L. Bottou. *Stochastic Gradient Descent Tricks*, pages 421–436. Springer Berlin Heidelberg, Berlin, Heidelberg, 2012.

[46] Manoj Kushwah and Ashis Patra. PID controller tuning using ziegler-nichols method for speed control of dc motor. In *International Journal of Scientific Engineering and Technology Research*, 06 2014.

[47] P. Pesek, S. Zvánovec, P. Chvojka, Z. Ghassemlooy, and P. A. Haigh. Demonstration of a hybrid FSO/VLC link for the last mile and last meter Networks. *IEEE Photonics Journal*, vol. 11:pages 1–7, Feb 2019.

[48] L. Xie, Y. Shi, Y. T. Hou, and A. Lou. Wireless power transfer and applications to sensor networks. *IEEE Wireless Communications*, vol. 20:pages 140–145, August 2013.

[49] Shlomi Arnon. Underwater optical wireless communication network. *Optical Engineering*, vol. 49:pages 1 – 6, 2010.

[50] Xiaoyan Liu, Suyu Yi, Xiaolin Zhou, Zhilai Fang, Zhi-Jun Qiu, Laigui Hu, Chunxiao Cong, Lirong Zheng, Ran Liu, and Pengfei Tian. 34.5 m underwater optical wireless communication with 2.70 gbps data rate based on a green laser diode with nrz-ook modulation. *Opt. Express*, vol. 25:pages 27937–27947, Oct 2017.

[51] Martin Chaplin. Absorption coefficient. `http://www1.lsbu.ac.uk/water/water_vibrational_spectrum.html`. Accessed: 2019-09-30.